Opto-Electronic Science

CN 51-1800/O4 ISSN 2097-0382 (Print) ISSN 2097-4000 (Online)

Optical scanning endoscope via a single multimode optical fiber

Guangxing Wu, Runze Zhu, Yanqing Lu, Minghui Hong and Fei Xu

Citation: Wu GX, Zhu RZ, Lu YQ, et al. Optical scanning endoscope via a single multimode optical fiber. *Opto-Electron Sci* **3**, 230041 (2024).

https://doi.org/10.29026/oes.2024.230041

Received: 9 November 2023; Accepted: 26 January 2024; Published online: 22 March 2024

Related articles

Speckle structured illumination endoscopy with enhanced resolution at wide field of view and depth of field

Elizabeth Abraham, Junxiao Zhou, Zhaowei Liu

Opto-Electronic Advances 2023 **6**, 220163 doi: 10.29026/oea.2023.220163

In-fiber photoelectric device based on graphene-coated tilted fiber grating

Biqiang Jiang, Yueguo Hou, Jiexing Wu, Yuxin Ma, Xuetao Gan, Jianlin Zhao

Opto-Electronic Science 2023 **2**, 230012 doi: 10.29026/oes.2023.230012

Specialty optical fibers for advanced sensing applications

Huanhuan Liu, Dora Juan Juan Hu, Qizhen Sun, Lei Wei, Kaiwei Li, Changrui Liao, Bozhe Li, Cong Zhao, Xinyong Dong, Yuhan Tang, Yihong Xiao, Gerd Keiser, Perry Ping Shum

Opto-Electronic Science 2023 **2**, 220025 doi: 10.29026/oes.2023.220025

Spatiotemporal hemodynamic monitoring via configurable skin-like microfiber Bragg grating group

Hengtian Zhu, Junxian Luo, Qing Dai, Shugeng Zhu, Huan Yang, Kanghu Zhou, Liuwei Zhan, Biao Xu, Ye Chen, Yanqing Lu, Fei Xu

Opto-Electronic Advances 2023 **6**, 230018 doi: 10.29026/oea.2023.230018

More related article in Opto-Electronic Journals Group website

OES Opto-Electronic Science

http://www.oejournal.org/oes

OE_Journal

Website

Opto-Electronic Science

Review

March 2024, Vol. 3, No. 3

DOI: 10.29026/oes.2024.230041

Optical scanning endoscope via a single multimode optical fiber

Guangxing Wu[1,2†], Runze Zhu[2†], Yanqing Lu[2], Minghui Hong[3*] and Fei Xu[2*]

Optical endoscopy has become an essential diagnostic and therapeutic approach in modern biomedicine for directly observing organs and tissues deep inside the human body, enabling non-invasive, rapid diagnosis and treatment. Optical fiber endoscopy is highly competitive among various endoscopic imaging techniques due to its high flexibility, compact structure, excellent resolution, and resistance to electromagnetic interference. Over the past decade, endoscopes based on a single multimode optical fiber (MMF) have attracted widespread research interest due to their potential to significantly reduce the footprint of optical fiber endoscopes and enhance imaging capabilities. In comparison with other imaging principles of MMF endoscopes, the scanning imaging method based on the wavefront shaping technique is highly developed and provides benefits including excellent imaging contrast, broad applicability to complex imaging scenarios, and good compatibility with various well-established scanning imaging modalities. In this review, various technical routes to achieve light focusing through MMF and procedures to conduct the scanning imaging of MMF endoscopes are introduced. The advancements in imaging performance enhancements, integrations of various imaging modalities with MMF scanning endoscopes, and applications are summarized. Challenges specific to this endoscopic imaging technology are analyzed, and potential remedies and avenues for future developments are discussed.

Keywords: multimode optical fiber; endoscope; scanning imaging; focusing; wavefront shaping

Wu GX, Zhu RZ, Lu YQ et al. Optical scanning endoscope via a single multimode optical fiber. *Opto-Electron Sci* **3**, 230041 (2024).

Introduction

Endoscopes are widely employed visual instruments in biomedicine, allowing in-depth, rapid and minimally invasive imaging of objects that cannot be directly accessed from surfaces. In clinical medicine, specialized endoscopes designed for various tubular or cavity organs, such as gastrointestinal tract, throat, nasal passages and brain ventricles, have been developed[1]. To alleviate the discomfort of patients during examination processes and enhance the reliability of diagnosis, medical endoscopes inherently demand continuous miniaturization, excellent spatiotemporal resolution, and high image quality. In life science, similar requirements are placed on endoscopes to achieve high-resolution imaging while minimizing invasiveness to the biological tissue or cells[2]. These application demands are driving the fast development of endoscopes. So far, diverse endoscopes based on different principles have been created and can be broadly categorized as follows: rigid lens endoscopes, electronic endoscopes, and optical fiber endoscopes[3]. Among them,

[1]Department of Electrical and Computer Engineering, National University of Singapore, 4 Engineering Drive 3, 117576, Singapore; [2]College of Engineering and Applied Sciences and Collaborative Innovation Center of Advanced Microstructures, Nanjing University, Nanjing 210023, China; [3]Pen-Tung Sah Institute of Micro-Nano Science and Technology, Xiamen University, 33 Qunxian Road, Xiamen 361005, China.

†These authors contributed equally to this work.

*Correspondence: MH Hong, E-mail: elehmh@xmu.edu.cn; F Xu, E-mail: feixu@nju.edu.cn

Received: 9 November 2023; Accepted: 26 January 2024; Published online: 22 March 2024

Open Access This article is licensed under a Creative Commons Attribution 4.0 International License.
To view a copy of this license, visit http://creativecommons.org/licenses/by/4.0/.

© The Author(s) 2024. Published by Institute of Optics and Electronics, Chinese Academy of Sciences.

optical fiber endoscopes have some unique advantages, including high flexibility, small probe size, ease of high-temperature sterilization, and resistance to electromagnetic interference, providing irreplaceable advantages in specific applications[4,5]. The inception of optical fiber endoscopes dates back to 1954 when Hopkins et al. pioneered their development[6,7]. This time even predates the proof that optical fiber could serve as a medium for extremely low-loss communication[8]. Optical fiber endoscopes can be categorized into fiber bundle endoscopes, single-mode fiber scanning endoscopes, or multimode fiber endoscopes, depending on the type of employed optical fiber.

The optical fiber bundle endoscope is the earliest fiber-based endoscope. Fiber bundles comprise numerous individual optical fibers, with each fiber independently transmitting one pixel of the image. As a result, the obtained image is presented in a pixelated form. Intuitively, the imaging resolution of fiber bundles depends on the size of the cores and the distance between adjacent cores. At present, commercially available optical fiber bundles have core radii around 1 μm and center-to-center spacings around 3 μm[9,10]. The single-mode fiber scanning endoscope is the other mature fiber-based endoscope. Single-mode optical fibers can only transmit optical energy because all spatial information carried by the incident light is merged into a single optical guiding mode. To focus light and conduct the scanning task, the distal end of the single-mode optical fiber is integrated with a two-dimensional microelectromechanical system (MEMS) mirror or a piezoelectric actuator and lens system[11–13]. The imaging properties of the single-mode optical fiber scanning endoscopes are significantly different from the fiber bundle endoscopes. The physical imaging resolution limit of this endoscope is determined by the point spread function of the lens system while its practical resolution in use depends on scanning motion and sampling rate[14,15]. A large field-of-view (FOV) of the single-mode fiber scanning endoscopes can be acquired by increasing the displacement of MEMS mirrors or the resonance amplitude of the fiber tip. The fiber bundle endoscope and the single-mode fiber scanning endoscope are both well-established endoscopic techniques and have been employed in many biomedical applications[16]. Regarding most imaging applications for relatively large tubular or cavity structures within the human body, the two fiber-based endoscopes already meet the demands effectively. However, when the target application involves some extreme scenarios, such as high-resolution in vivo imaging of deep brain areas and tubular structures with only a few hundred micrometers in size, such as the Schlemm's canal in the human eye[17], they are currently not suitable. In such application scenarios, the footprints of fiber bundle endoscopes and single-mode optical fiber scanning endoscopes are relatively large, preventing them from accessing the desired area of samples for imaging or creating substantial mechanical lesions of the tissues[10,18]. Besides, the fiber bundle endoscopes face the challenge related to the imaging resolution, which is restricted by the distance of different fiber bundle cores and the fabrication crafts[19–21]. In this context, MMF-based endoscopes are potential solutions for these applications.

Unlike single-mode optical fibers, multimode optical fibers (MMF) support the transmission of numerous guided modes, offering a large number of degrees of freedom for manipulating the optical field and thereby allowing for all-optical scanning[22]. As illustrated in Fig. 1, focused light spots at the distal end of an MMF are attained by employing a spatial light modulator (SLM) to perform wavefront shaping on the incident optical field[23,24]. The wavefront shaping information used to modulate light for focusing can be acquired by transmission matrix measurements, digital phase conjugate methods and phase optimization algorithms[22,25,26]. So far, the MMF scanning endoscope (MFSE) has achieved diffraction-limited foci and submicron imaging resolution. When compared to the optical fiber bundle, the effective pixel density delivered by an MMF can be significantly higher[25,27]. Moreover, the MFSE focuses light in an all-optical manner without integrating lenses or actuators at the distal end of the MMF. Therefore, the size of the endoscope probe is only determined by the diameter of the MMF, which is smaller than the probe of the single-mode fiber scanning endoscope. Certainly, it should be highlighted that the MMF-based endoscopes are still in development and are not yet operational in practical applications. There are still some issues that need to be addressed in the MFSE technique. For example, the scanning imaging performance of MFSE is highly susceptible to external dynamic disturbances and the deformation of MMF. Besides, the entire calibration and imaging apparatus of MFSE is complex. Therefore, substantial efforts are still needed to promote the practical applications of MFSE.

In this article, the optical scanning endoscope using a

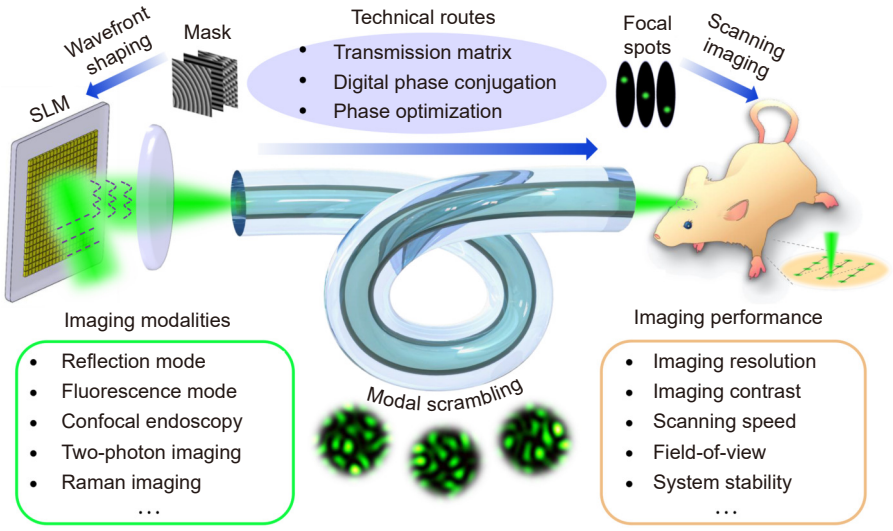

Fig. 1 | Schematic of MFSE based on wavefront shaping technique. The upper part illustrates three technique routes to acquire appropriate masks for wavefront shaping, aiming at generating high-quality focal spots at the output end of MMF for scanning imaging. The bottom two boxes illustrate the developments of MFSE, including improving imaging performance and combining the MFSE with diverse advanced imaging modalities.

single MMF based on the wavefront shaping technique is comprehensively reviewed. Notably, in addition to generating tightly focused light spots for scanning imaging, there are some other imaging mechanisms to achieve endoscopic imaging through the MMF[28], including wide-field imaging by inverse methods[29–31], compressive imaging technique[32–34] and deep learning-based imaging methods[35–38]. Each of endoscopic imaging techniques grounded in these mechanisms possesses a wealth of research content. To avoid excessive diversification of topics without in-depth exploration, in this review, we only focus on MMF scanning imaging using focused light spots. Compared to these alternative imaging mechanisms, MFSE is relatively more mature and can be applied to complex imaging scenarios. Many advanced imaging modalities, such as confocal endoscopy, two-photon imaging, Raman imaging and photoacoustic imaging, can be integrated with the MFSE system to achieve comprehensive enhancement of imaging capacity. The contents of this review are illustrated in Fig. 1 and arranged as follows. Section *Principle of multimode optical fiber scanning endoscope* introduces the three technical routes to generate focused light spots through MMFs and the scanning imaging process of MFSEs. Section *Scanning imaging performance* analyzes several key scanning imaging performance metrics of MFSE and introduces strategies to improve these metrics. In Section *Different scanning imaging modalities*, integrations of MFSEs with other advanced scanning imaging modalities and the corresponding performance improvements are outlined. In Section *Applications*, the progress of MFSE in applications is introduced. Challenges faced in the current MFSE system and the prospects of this technology are analyzed in Section *Challenge and outlook*, followed by a summary presented in the last section.

Principle of multimode optical fiber scanning endoscope

Optical field propagation properties of MMF

Over the past decade, considerable attention has been devoted to the development of endoscopes based on a single MMF. As the name implies, MMFs can support the propagation of numerous eigenmodes. The number of eigenmodes supported by a specific MMF is determined by the core radius a of the optical fiber, the refractive indices of the core and cladding, and the wavelength λ of the incident light. Commonly, MMFs are categorized into step-index and graded-index MMFs based on different refractive index distributions. In the case of step-index MMFs, the number of modes can be estimated using the following formula (Chapter 8, pages 293 of ref.[39]):

$$N \approx \frac{1}{2}\left(\frac{2\pi a}{\lambda}\right)^2 (n_1^2 - n_2^2) \ , \tag{1}$$

where n_1 and n_2 are the refractive indices of the core and cladding of the optical fiber, respectively. In the case of graded-index MMFs, their cores typically conform to the following refractive index profiles (Chapter 8, page 288 of ref.[39]):

$$n^2(r) = n_1^2\left[1 - 2\left(\frac{r}{a}\right)^p\left(\frac{n_1^2 - n_2^2}{2n_1^2}\right)\right], \quad (2)$$

where n_1 is the maximum refractive index value inside the core and n_2 is the refractive index of the cladding. r is the distance from a specific point inside the core to the center. p is a parameter that determines the steepness of the graded-index profile. The number of modes supported by this kind of graded-index MMF can be estimated using the following formula (Chapter 8, page 293 of ref.[39]):

$$N \approx \frac{1}{2}\frac{p}{p+2}\left(\frac{2\pi a}{\lambda}\right)^2(n_1^2 - n_2^2). \quad (3)$$

The graded-index MMFs typically exhibit lower modal dispersion and better resistance to external disturbances. Therefore, they are generally preferred in the MMF scanning imaging applications.

In practical usage, the modes excited within an MMF are determined by the relative position and angle of the incident light field with respect to the input face of the optical fiber. The excited eigenmodes propagate within the MMF with different propagation constants, leading to what is known as modal dispersion as illustrated in Fig. 2. When an optical field carrying ordered information enters an MMF, it is transformed into a series of eigenmodes. During the propagation process, mode coupling may occur among these eigenmodes due to non-uniformities of the MMF along the propagation direction or external disturbances. At the output end of MMF, the phase differences, relative amplitudes and polarization states among these eigenmodes become completely different from the initial state due to the modal dispersion and mode coupling effects[40]. As a result, the total optical field formed by the superposition of various eigenmodes exhibits a speckled distribution at the output end of MMF. The information carried in the optical field is also scrambled. Therefore, MMFs are not suitable for direct image transmission or the formation of focused light spots. To obtain a focused light spot for scanning imaging through the MMF, measures must be taken to proactively compensate for the information distortion caused by the modal dispersion and mode coupling.

Technical routes for light focusing

So far, to generate focused light spots through MMF for scanning imaging, numerous techniques have been put forth to counteract the modal scrambling properties of MMF based on the wavefront shaping principle. These techniques include the transmission matrix measurement method, digital phase conjugation method and phase optimization algorithms. Next, we will introduce these techniques in detail.

Transmission matrix measurement method

The transmission matrix measurement method was initially developed to enable the use of disordered media for imaging applications[31,41]. Because of the resemblance between the modal dispersion in MMFs and the linear scattering effect in disordered media, it was adapted for use in the realm of MMF endoscopic imaging. In this method, the MMF is regarded as a linear system. The input and output ends of the optical fiber are divided into a series of orthogonal spatial modes by a square grid as illustrated in Fig. 3(a). If the optical field is excited in a specific spatial mode at the input end, the response including amplitude and phase of the optical field at the output end, i.e. the pulse response function of the linear system, can be measured. Once the responses at the output end for all input modes are acquired, we obtain the complete transmission matrix $\boldsymbol{T}_{mn}$ of the MMF, which can be used to calculate the output optical field $\boldsymbol{E}_m^{\text{out}}$ corresponding to arbitrary input optical field $\boldsymbol{E}_n^{\text{in}}$ by formula:

$$\boldsymbol{E}_m^{\text{out}} = \boldsymbol{T}_{mn} \cdot \boldsymbol{E}_n^{\text{in}}, \quad (4)$$

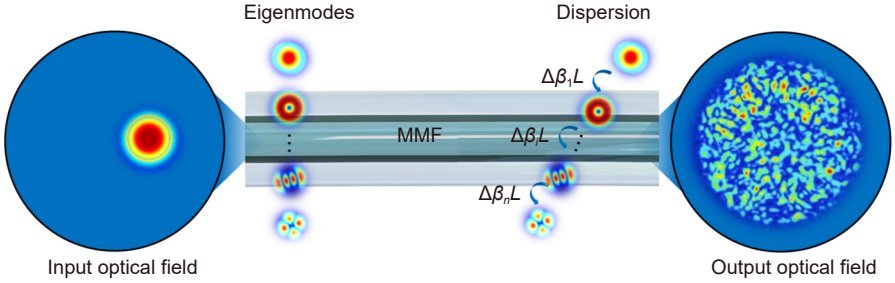

Fig. 2 | Schematic of optical fields propagating through an MMF. Due to the modal dispersion and mode coupling of the MMF, the input optical field with an ordered profile is converted into a speckled output optical field. $\Delta\beta L$ represents the phase differences between different eigenmodes caused by the intermodal dispersion.

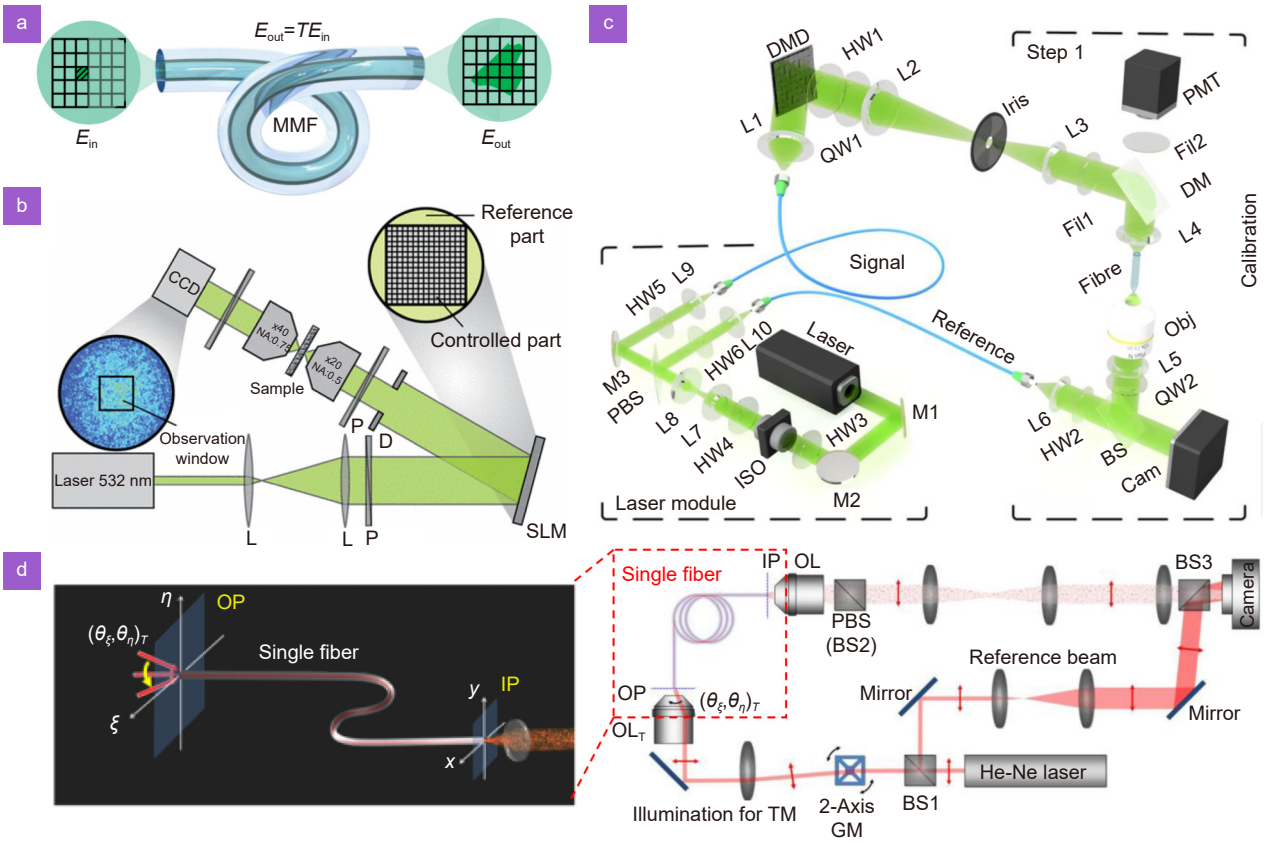

Fig. 3 | (**a**) Schematic to illustrate the definition of the transmission matrix of an MMF. Schematics of experimental setups to measure the transmission matrix of MMF or disordered media using (**b**) internal and (**c**) external references. (**d**) Schematic of the experimental setup to measure the transmission matrix through the spatial frequency domain method. Figure reproduced with permission from: (b) ref.[41], American Physical Society; (c) ref.[42], Springer Nature, under a Creative Commons Attribution 4.0 International License; (d) ref.[29], American Physical Society.

where $\boldsymbol{E}_n^{\text{in}}$ and $\boldsymbol{E}_m^{\text{out}}$ are column vectors, in which each element represents the complex amplitude of the corresponding spatial modes. Each column of $\boldsymbol{T}_{mn}$ corresponds to the measured pulse response function for a specific input spatial mode. In the MFSE, it is desired to generate a series of focal spots at the output end of the MMF for scanning imaging. The wavefront shaping information to generate focal spots is first derived by calculating the inverse of the transmission matrix. Subsequently, it is loaded onto the input optical field of the MMF by an SLM. Therefore, the cornerstone of this technical route lies in the precise measurement of the transmission matrix.

Generally speaking, the transmission matrix $\boldsymbol{T}_{mn}$ is a complex matrix, in which the magnitudes and arguments of the elements represent the amplitude and phase of the response optical field for a given input spatial mode, respectively. If cameras are used to record the response optical field, only the intensity can be measured and the phase information is lost. To obtain the phase profile of the response optical field at the output end of MMF, full-field interferometric methods are often adopted. Schematics of optical paths to measure the complex transmission matrix of MMF or disordered media using internal and external references are presented in Fig. 3(b) and 3(c), respectively. In the case of using an internal reference optical path, light from a portion of the wavefront shaping device, such as a liquid crystal spatial light modulator (LC-SLM) or a digital micro-mirror device (DMD), is held constant and directed into the MMF as the reference light. Light from other spatial modes is sequentially incident into the MMF and interferes with the reference light. When the modulation device is an LC-SLM, a blazed phase grating should be loaded at the tested spatial mode to ensure that its first-order diffracted pattern precisely enters the MMF while light from the other spatial modes without the modulation of blazed phase grating is blocked by the aperture and does not participate in interference[23]. If the DMD is employed, it should be encoded with a specific binary amplitude Lee hologram[43]. To derive the phase of the response optical field from the interference pattern, phase-shifting interferometry is commonly employed, such as the two-

phase, three-phase and four-phase methods[41,44–46]. The four-phase method is widely used as it does not require prior measurements of the intensities of the response optical fields. According to the four-phase method, the phase profile φ_{mn} of the response optical field can be calculated by

$$\varphi_{mn} = \arctan\left[\frac{I_{mn}^{3\pi/2} - I_{mn}^{\pi/2}}{I_{mn}^{0} - I_{mn}^{\pi}}\right], \tag{5}$$

where I_{mn}^{0}, $I_{mn}^{\pi/2}$, I_{mn}^{π} and $I_{mn}^{3\pi/2}$ are the interference intensities in the m^{th} output mode when the phase differences between the reference light and the n^{th} tested spatial mode are shifted by 0, $\pi/2$, π and $3\pi/2$. As such, if the intensity of the reference light is also measured in advance, both the magnitude and argument of the complex transmission matrix can be obtained. The internal reference method adopts a common pathway geometry and has the advantages of a simple measurement setup and insensitivity to environmental noise during the calibration processes. However, the internal reference method inherently has some problems. For example, the interference light also passes through the MMF, resulting in a speckle-like reference pattern. In the speckle pattern, some positions do not have sufficient optical power, which causes strong measurement errors with the phase-shifting interferometry and leads to "blind spots" in the obtained transmission matrix. Besides, the polarization parameter is not easy to optimize in this method[23,47]. Recently, Jákl et al. demonstrated that the problem of "blind spots" can be mitigated by conducting multiple measurements of the transmission matrix using various internal references[48,49]. In the study of Collard et al., they selected some internal reference beams with more uniform amplitude profiles in the interference plane to conduct the calibration and achieved a higher focusing efficiency with the measured transmission matrix[50].

As an alternative, the external reference optical path was also employed to measure the transmission matrix, circumventing certain issues inherent to the internal reference method. A typical calibration optical path of the external reference method is displayed in Fig. 3(c). The reference light propagates in a single-mode fiber and generates a Gaussian beam with relatively uniform intensity distribution to interfere with the light output from the MMF, thereby eliminating problems with "blind spots". However, since the reference and test light propagate in different optical pathways, mechanical and thermal drifts of the setup during the calibration process potentially led to the instability of the measurement results. To ensure the stability of the phase relationship between individual optical pathways, employing a feedback loop is essential, which adds complexity to the calibration apparatus. Besides, to promote the contrast of the interference pattern, the intensity of the reference light should be properly selected. Internal and external reference methods each have their unique advantages and disadvantages when measuring the transmission matrix, so the choice should be made based on the specific circumstances.

Except for the above spatial domain measurement method, transmission matrices can also be measured in the spatial frequency domain. The experimental setup operating in the spatial frequency domain is displayed in Fig. 3(d)[29]. In the spatial frequency domain, input modes of an MMF consist of a series of plane waves with various incident angles, rather than the point sources arranged in a square grid used in the spatial domain. Correspondingly, a two-axis galvanometer scanning mirror instead of the SLM is exploited to change the incident angle of plane waves in the experimental setup. Using the setup presented in Fig. 3(d), the response optical field $\boldsymbol{E}_{\text{fiber}}(x, y; \theta_\xi, \theta_\eta)$ for each plane wave with angles $(\theta_\xi, \theta_\eta)$ can be acquired. This response optical field measured in the frequency domain cannot be directly used for wavefront shaping with SLMs. It is necessary to convert the frequency domain input-output responses into the form of a transmission matrix in the spatial domain using the following equation[29]:

$$\boldsymbol{T}(x, y; \xi, \eta) = \sum_{\theta_\xi, \theta_\eta} \boldsymbol{E}_{\text{fiber}}(x, y; \theta_\xi, \theta_\eta)\, \boldsymbol{E}(\theta_\xi, \theta_\eta; \xi, \eta), \tag{6}$$

where $\boldsymbol{E}(\theta_\xi, \theta_\eta; \xi, \eta)$ is the output optical field at $(\theta_\xi, \theta_\eta)$ for an incident light at (ξ, η). It can be acquired by inverting the matrix $\boldsymbol{E}(\xi, \eta; \theta_\xi, \theta_\eta)$. The coordinate system that defines these variables in Eq. (6) is displayed on the left of Fig. 3(d). Based on Eq. (6), the spatial frequency domain measurements can be exploited to focus light in the same way as the transmission matrix measured in the spatial domain.

When the above methods are used to acquire the transmission matrix, the optical response (i.e. one column of the transmission matrix) of each input spatial mode needs to be measured one by one. However, if the employed MMF has perfect cylindrical geometry, the optical responses corresponding to input spatial modes at the same radial radius should exhibit rotational symmetry,

which can be exploited to accelerate the measurements of transmission matrices. Specifically, once the optical response of an input spatial mode is obtained, it can be used to calculate the optical responses of other spatial modes located in a circle through a rotation operator, significantly reducing the calibration time. In 2015, Amitonova et al. demonstrated that the rotational memory effect in an MMF can be used for ultrafast high-resolution scanning imaging[51]. Using the wavefront shaping information of one focused light spot, they enable the rotation of the focal spot across a 360° range with minimal change in spot size throughout the entire rotation process. Unfortunately, there is significant variation in the power of the focal spot from 4% to 40% during the rotation. Further, Li et al. proposed a more general framework describing memory effects in MMF. They identified a quasi-radial memory effect in MMFs and demonstrated that the transmission matrix can be estimated approximately by placing a guide star at the output end of the MMF as a feedback tool[52]. However, this method is sensitive to the rotational symmetry of the refractive index distribution and the geometry of MMF. If the MMF is disturbed, only partial data in the estimated transmission matrix remains valid, specifically related to the optical field responses near the guide-star region.

In addition to using interferometric methods to acquire elements in the transmission matrix, some researchers also employ optimization algorithms to obtain the complex transmission matrix only with measured intensities of the output optical fields. In 2015, Drémeau et al. utilized a Bayesian phase retrieval algorithm to estimate the transmission matrix, leveraging experimental intensity measurements with inherent noise[53]. In 2018, N' Gom et al. proposed a semidefinite program to generate the transmission matrix using intensity-only measurements[54]. They randomly generated some wavefronts and input them into the MMF. By feeding back intensities of the output optical fields into the PhaseCut-based convex optimization algorithm, they can obtain the corresponding row of the complex transmission matrix one by one. In the same year, Deng et al. introduced a phase retrieval algorithm based on Bayesian inference to estimate the transmission matrix, offering the potential for acceleration through distributed or parallel computation[55]. In 2019, Caramazza et al. introduced an iterative optimization approach for statistically reconstructing the complex inverse transformation matrix of MMF based on a physically informed model[56]. In 2020, Huang et al. presented an approach to recursively search for the transformation matrix based on an extended Kalman filter and a modified speckle-correlation scatter matrix[57]. Using these optimization algorithms to acquire the transmission matrix of MMF has the advantage of a simple calibration setup. However, the fidelity of the transmission matrix obtained by these algorithms is inferior to that acquired by interferometric measurements and thus the quality of focal spots is degraded.

Transmission matrices obtained by all the above methods are complex, allowing the full modulation of both amplitude and phase of the optical field. For the sake of simplicity, there are also some works studying the real-valued transmission matrix for light focusing through MMF. The real-valued transmission matrix can directly connect the intensities of input and output modes. This simplified approach is specifically developed when a DMD is employed as the SLM. As we have mentioned above, if a DMD is used to conduct the complex modulation of the optical field, Lee hologram method should be adopted. However, considering that DMD fundamentally controls the "ON" and "OFF" states of individual micromirrors for wavefront shaping, it can also directly establish a binary transmission matrix to connect the relationship between the focused optical field and the binary states of micromirrors. In 2015, Tao et al. proposed a method to directly calculate the binary transmission matrix using the measured light intensities in the image plane, which were modulated by a series of masks designed with Hadamard basis on the DMD[58]. This method does not rely on measured intensities as feedback information for iterative optimization. Therefore, it achieved a very short calibration time, i.e. 75 ms for 1024 input modes. In 2018, Zhao et al. presented a high-speed algorithm based on Bayes' theorem to estimate the binary transmission matrix[59]. The conditional probability of each micromirror contributing positively to the desired focal spot, when it is in the "ON" state, is calculated. Then, only those micromirrors whose probabilities exceed a defined threshold are set in the "ON" state. This method can calibrate one row of the transmission matrix in 0.26 s for 5000 input-output pairs. In 2020, they further reported a real-valued intensity transmission matrix to characterize relationships between input and output light intensities of MMF[27]. This transmission matrix was derived based on an assumption of pseudo-linearity between the input and output intensity distributions. In 2021, they provided a comprehensive

comparison of some transmission matrix estimation approaches[60]. Compared to the complex modulation using DMD, the binary intensity modulation offers higher efficiency in utilizing light energy while the produced focal spots exhibit inferior contrast. Besides, the system employed for the calibration of the binary transmission matrix is simpler.

After measuring the transmission matrix, the appropriate mask is calculated for SLM to reshape the wavefront of the input optical field. Ideally, we can set $\boldsymbol{E}_m^{\text{out}}$ as the optical field distribution of the desired output focal spot, and the corresponding mask can be obtained by calculating the inverse $\boldsymbol{T}_{mn}^{-1}$ of the measured transmission matrix[29]:

$$\boldsymbol{E}_n^{\text{in}} = \boldsymbol{T}_{mn}^{-1}\boldsymbol{E}_m^{\text{out}} \ . \tag{7}$$

However, noise is inevitably present during the practical measurement process. In such a situation, the matrix inversion operator may introduce singular values, leading to a significant deviation of the calculated mask from the expected outcome. To address this problem, a more general scheme is exploiting optimization methods to calculate the mask. When the mean square optimized operator is adopted, the mask can be calculated by[31]:

$$\boldsymbol{E}_n^{\text{in}} = \left(\boldsymbol{T}_{mn}^{\dagger}\cdot\boldsymbol{T}_{mn} + \sigma\cdot\boldsymbol{I}\right)^{-1}\boldsymbol{T}_{mn}^{\dagger}\boldsymbol{E}_m^{\text{out}}, \tag{8}$$

where σ is the standard deviation of noise and $\boldsymbol{I}$ is an identity matrix. Based on Eq. (8), the incident optical field with the desired wavefront can be shaped using an SLM. In the case of pure phase modulation, the amplitude of the incident optical field $\boldsymbol{E}_n^{\text{in}}$ can be directly ignored and its phase distribution is used as the modulation mask. Notably, when amplitude modulation is not employed and all modes are set with a constant amplitude, the focusing efficiency decreases to approximately 78.5%[23]. Besides, if the input polarization is not controlled, only 50% of the input modes, on average, can be constructive interference at the designated focal point. Therefore, some researchers designed complex optical paths to measure the optical response of different polarizations in MMF and subsequently exploited the polarization information to achieve a higher focusing efficiency[23,25,61].

Digital phase conjugation method

Phase conjugation is an effective technique to eliminate the image distortion caused by inhomogeneous media during the transmission process[62–64]. Traditional optical phase conjugation techniques were primarily implemented using photorefractive crystals and had been applied to image transmission through MMFs for several decades[65]. However, this method has several drawbacks. Photorefractive crystals are wavelength-selective and have a slow response time. Besides, the optical phase conjugation setup is complex, often requiring two identical optical fibers, which can be challenging to achieve in practical applications[66]. Recently, the emergence of pixelated SLM has made the digital phase conjugation technique a preferred choice for wavefront corrections.

In 2011, Papadopoulos et al. first applied the digital phase conjugation technique to focus light through an MMF[22,67]. A typical experimental setup to realize the digital phase conjugation in an MMF is displayed in Fig. 4(a). The implementation process generally involves four steps, as illustrated in Fig. 4(b). Firstly, a light spot is focused onto the proximal facet of the MMF as the excitation through an objective. Secondly, the excitation light transmits through the MMF, generating a speckle pattern at the output end. The output optical field interferes with a reference light beam, resulting in an interference pattern, which is recorded on a CMOS detector. Thirdly, the recorded interference pattern is exploited to reconstruct the amplitude and phase information of the output optical field with some numerical calculations[68,69]. Finally, the calculated phase is loaded into the SLM for wavefront reshaping. As shown in Fig. 4(a), a portion of the reference light is separated and modulated with the phase mask on the SLM before being reflected into the MMF. After this conjugate wave travels back through the MMF, a focused light spot at the initial input facet is formed. Using the digital phase conjugation technique, Papadopoulos et al. achieved a focused beam with a waist of 2.25 μm and an enhancement factor of 1800. They also conducted validation experiments for scanning endoscopic imaging using fluorescent beads and biological samples[70]. In 2018, Ma et al. exploited the rotational memory effect of MMF to reduce the measurements of conjugated phase masks and thus boost the calibration speed[69]. They achieved focused light spots with a full-width at half-maximum (FWHM) of 1.3 μm and an enhancement factor of 900.

Despite the substantial potential of the digital phase conjugation technique in the MFSE, its practical use is constrained by several significant problems. Firstly, precise pixel-to-pixel alignment between the SLM and

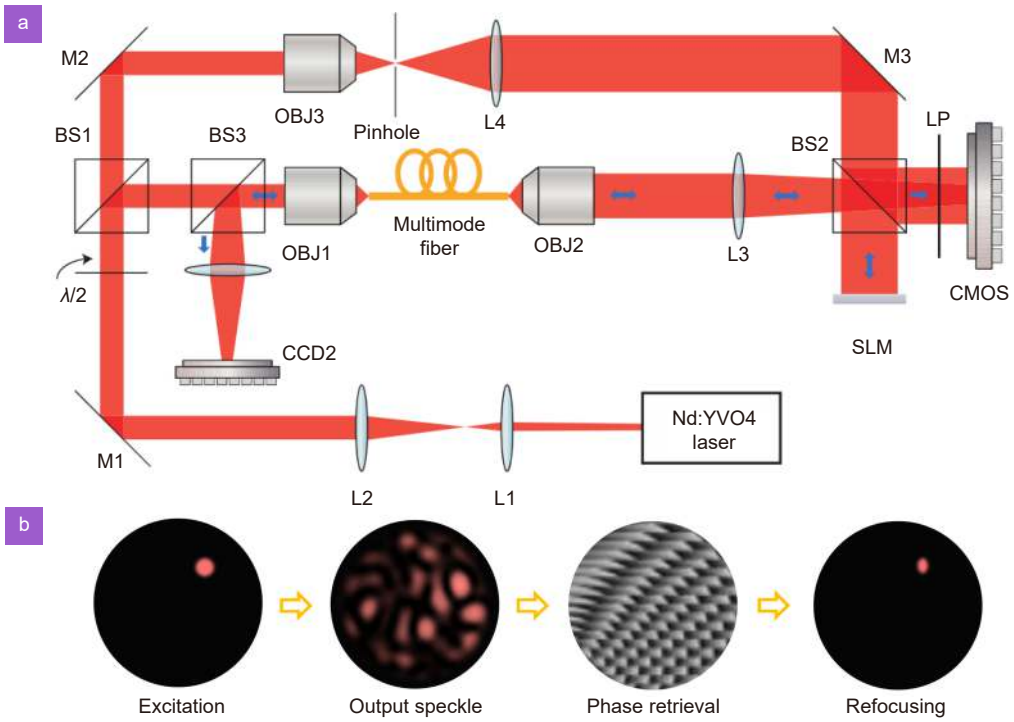

Fig. 4 | (**a**) Schematic of the experimental setup to implement digital phase conjugation through an MMF, (**b**) illustration of four steps to realize light focusing through an MMF based on the digital phase conjugation principle. Figure (a) reproduced with permission from ref.[22], © Optica Publishing Group.

image sensor is required, which is the prerequisite to forming the correct phase conjugate beam. Secondly, the phase conjugate beam and the initial light beam output from the MMF need to be precisely superimposed. The two alignment problems are challenging and critical to generate high-quality focal spots. To facilitate the alignment between the SLM and CMOS camera, Ma et al. suggested adding a 4f system between the SLM and CMOS camera[69]. This modification simplifies the alignment process by imaging the grayscale pattern from the SLM onto the CMOS camera. Mididoddi et al. later proposed a transmission matrix-assisted calibration method to relax the stringent alignment criteria between the SLM and the CMOS camera[71]. To achieve a good overlap between the phase conjugate beam and the light beam output from the MMF, the tilt parameters of mirror M3 in Fig. 4(a) should be well adjusted. Jang et al. also proposed an auto-alignment method for the digital phase conjugation system using a digital propagation method[72]. Anyway, to maintain the alignment state, both mechanical and thermal stabilities of the imaging system based on digital phase conjugation are required to be high enough.

Phase optimization method

The two methods introduced above rely on intricate optical systems for measuring the propagation properties of MMFs, thereby obtaining wavefront shaping masks to generate focal spots. Unlike these two hardware-based methods, the phase optimization method focuses on algorithmic efforts to directly search for masks that can generate the desired focal spots. During the optimization process, the SLM is divided into several subregions. The phase of each subregion is optimized through iterative algorithms with the focusing intensity or contrast at the desired position as the metric of performance. Research in this direction is focused on updating iterative optimization algorithms, such as the Monte-Carlo algorithm[26], adaptive sequential coordinate ascent algorithm[73], stochastic parallel gradient descent algorithm[74], self-adaptive genetic algorithm[75], and natural evolution strategy[76] to simultaneously reduce the time of calibration and acquire more effective masks for the generation of high contrast focal spots. These algorithms can be divided into two categories. One of them uses speckle intensity measurements to facilitate the search for optimal masks, while the other relies on interference measurements.

In terms of the first category, in 2011, Leonardo et al. first presented the usage of the phase optimization method to produce focal spots through MMF[26]. They conducted

the direct search of phase mask by a Monte-Carlo algorithm in the reciprocal space of SLM, which takes ~10 minutes to complete an optimization process for a 2 m MMF. The generated focal spot occupies 14% of the total power. However, this direct search strategy is sensitive to the perturbation of MMFs. Recently, Yu et al. proposed a self-adaptive genetic algorithm capable of handling sudden and intense disturbances originating externally. Their experimental results indicate that it enhances the capability of MMF to refocus light with better contrast when the MMF experiences perturbations[75]. Later, Cheng et al. proposed a natural evolution strategy based on the natural gradient ascent to accelerate the global search for optimal wavefront shaping masks[76]. It takes 18 s to complete 2000 iterations for a single image projection in a 15 m MMF. The enhancement factor of the projected image is ~14. It is demonstrated that the anti-interference and convergence performance of this algorithm is better than other algorithms, including the particle swarm optimization method[77], genetic algorithm[78], and improved ant colony algorithm[79]. To note, the later three algorithms used for comparison were initially developed for light focusing through a disordered medium. It can be seen that most algorithms used for focusing light fields in disordered media can be applied to the MMF case. Comprehensive performance comparisons among various algorithms developed for disordered media, which also may be suitable for the light focusing of MMF, can be found in a study conducted by Fayyaz et al. in 2019[80].

The second category of phase optimization techniques is based on interference measurements, which can effectively reduce the total optimization time to generate a series of focal spots. The experimental part for these interference-based optimization methods is very similar to that adopted for measuring transmission matrices of MMF. In the experiment, the incident and output optical fields are partitioned into a series of square orthogonal modes on the SLM and the output facet of the MMF, respectively. As shown in Fig. 5(a–d), a spatial mode is selected as the internal reference light. The remaining spatial modes are individually guided into the MMF as the test light and sequentially interfere with the internal reference light. During the interference process, the phase of the test light is altered to traverse the range from 0 to 2π, and all interference patterns are recorded. Comparing these interference patterns, the phase at which the test mode contributes most to the intensity of

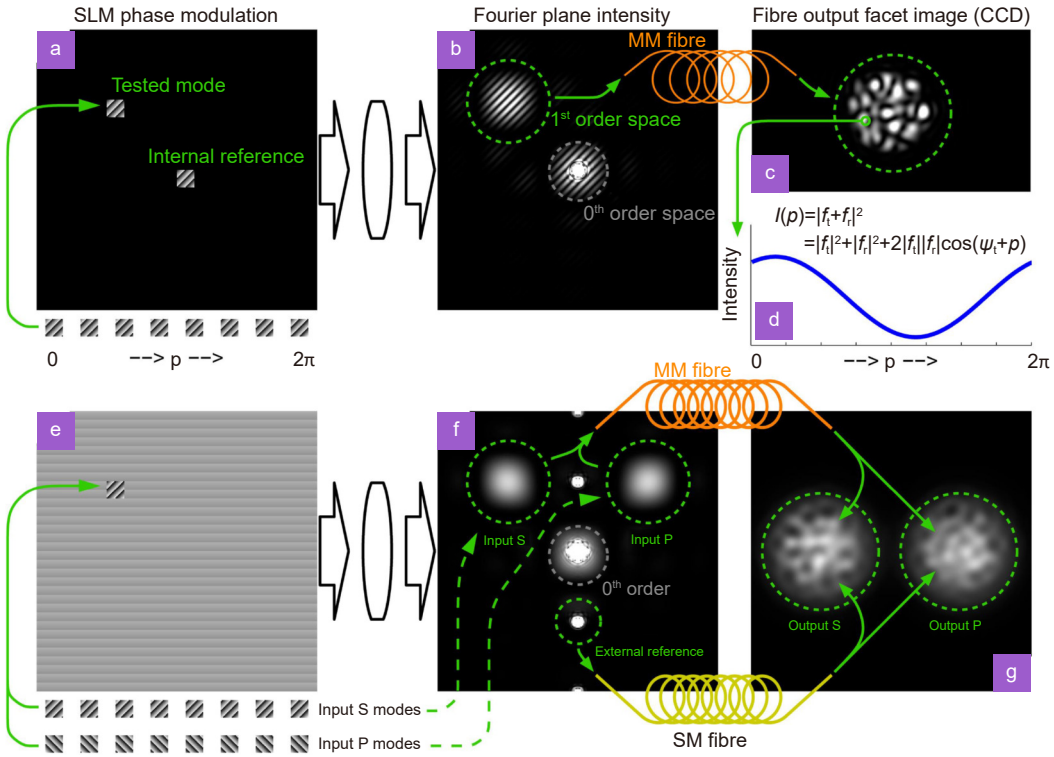

Fig. 5 | Principle of the interference-based optimization method. Optimization procedures based on (**a–d**) internal and (**e–g**) external reference pathways, respectively. When the external reference pathway is exploited, the effect of polarization on the light focusing can be comprehensively analyzed. Figure reproduced with permission from ref.[23], © Optica Publishing Group.

any desired output mode can be determined. Once all input modes have been tested, we can extract the phase mask required to focus light at any desired output mode. This optimization process can simultaneously yield the phase mask required for focusing light at any position on the output facet of the MMF, which distinguishes it from the optimization algorithms based on speckle intensity measurements. Besides, when the external reference pathway is exploited in the optimization procedure as shown in Fig. 5(e–g), the effect of all the parameters including phase, amplitude and polarization on light focusing can be fully analyzed. Based on the optimization for all these parameters, Čižmár et al. generated focal spots carrying 80% of the total power[23]. In 2015, Yin et al. proposed an adaptive parallel coordinate algorithm to reduce the calibration time in the interference-based optimization method[81]. Rather than exhaustively recording interference patterns of reference and test light at phase differences varying from 0 to 2π, they employed a three-phase shifting method to compute the relative phase between the reference and test light. Then, the optimal phase of test light to achieve the focus of light at a desired position can be obtained through calculations based on the interference formula. The three-phase shifting method was previously applied in the adaptive sequential coordinate ascent algorithm to optimize the phase mask[73]. However, it is slower than the adaptive parallel coordinate algorithm. Later, Chen et al. adopted a similar principle to optimize the phase mask with a two-phase shifting method[82,83]. It is evident that using phase shifting in conjunction with data processing greatly reduces the time required for experimental measurements, as compared to the phase enumeration manner. As outlined above, these interference-based phase optimization methods, particularly the adaptive parallel coordinate algorithm, share many similarities with the transmission matrix method, both in terms of experimental setups and data processing. Therefore, the calibration time of these interference-based phase optimization methods is comparable with the transmission matrix method.

Finally, in order to intuitively compare the focusing performance of MMFs based on different calibration techniques, the properties of focal spots reported in some representative works along with the experimental details are summarized and presented in Table 1. These subdivided technical routes include interferometric measurements of transmission matrix (TM-I), transmission matrix derived by optimization algorithm (TM-A), real-valued intensity transmission matrix (TM-R), digital phase conjugation (PC), digital phase conjugation combined with rotational memory effect (PC-R), phase optimization method based on speckle intensity (PO-S) and interference (PO-I) measurements. Here, we are concerned with two parameters of the focused light spot, i.e. the size and the contrast, which have a significant impact on the scanning imaging performance. The size of a focal spot is mainly measured by its FWHM while its contrast is characterized by the enhancement factor (η) or the power ratio (PR). The enhancement factor is the ratio between the peak intensity of the focal spot and the average intensity of the background. The PR represents the proportion of optical power contained in the focal spot relative to the total power transmitted through the

Table 1 | Focusing performance of MMFs based on different techniques.

Techniques	Experimental details	FWHM	Contrast	Refs
TM-I	L=15 cm, NA ~0.22, D= 50 μm; λ= 633 nm; DMD/complex modulation	~1.76 μm	PR=96% η=20000	ref.[84]
TM-A	L=1 m, NA ~0.2, D= 50 μm; λ= 642 nm; LC-SLM /phase-only modulation	—	η=286	ref.[57]
TM-R	L=1 m, NA ~0.22, D= 105 μm; λ= 532 nm; DMD/intensity modulation	~1.7 μm	η=89.4	ref.[60]
PC	L=1 m, NA ~0.22, D= 105 μm; λ= 1064 nm; LC-SLM /phase-only modulation	Beam waist ~2.25 μm	η=1800	ref.[22]
PC-R	L=18 cm, NA ~0.22, D= 105 μm; λ= 532 nm; LC-SLM / phase-only modulation	~1.3 μm	η=900	ref.[69]
PO-S	L=1 m, NA ~0.22, D= 200 μm; λ=532 nm; LC-SLM / phase-only modulation	—	η=71	ref.[75]
PO-I	L=1 m, NA ~0.22, D= 50 μm; λ=1064 nm; LC-SLM /complex modulation	—	PR=83%	ref.[23]

L: length of MMF, D: core diameter of MMF, λ: wavelength of light.

fiber. According to the data presented in the table, the sizes of focal spots produced by different techniques under various experimental conditions exhibit some differences, but they are not particularly significant. The differences in the focusing performance based on different techniques are primarily reflected in the contrast of focal spots. These techniques based on interferometric measurements, such as TM-I, PC, PC-R, and PO-I, can generate focal spots with significantly higher contrast compared to those acquired by other non-interferometric methods. These results indicate that techniques based on interferometric measurements can more accurately capture the modal scrambling properties of MMFs, thus enabling more effective wavefront shaping to generate focal spots. This is the reason that calibration techniques based on interferometric measurements remain the mainstream methods to obtain wavefront shaping masks. Among all techniques, the TM-I method has achieved the highest contrast of focal spots using a complex modulation. More details about how to achieve this optimal focusing performance are discussed in Section *Scanning imaging performance*. Although techniques based on non-interferometric measurements, such as TM-A, TM-R, and PO-S, do not yield very good focal contrast, they are advantageous in simple measurement setups and high temporal stability. These methods offer budget-friendly options in scenarios where high imaging performance is not necessary.

All-optical scanning imaging

Once the calibration for the MFSE is completed by these introduced techniques, masks to shape the wavefront for the generation of focal spots can be acquired and stored for subsequent scanning imaging applications. The experimental setup exploiting the stored masks for all-optical scanning imaging is displayed in Fig. 6(a). To note, this setup is used for the most common reflection or fluorescence imaging mode and setups for other imaging modalities will be discussed in Section *Different scanning imaging modalities*. The optical path used for calibration with different techniques is also ignored in this schematic. The light beam from the laser is expanded to cover the required modulation region on the SLM. Then, the wavefront of the light beam is modulated by the SLM with a certain stored mask. Subsequently, the modulated light beam located at the first diffraction order passes through an aperture and is coupled into the MMF through an objective lens. After the light beam exits the MMF, it forms a focal spot on a plane determined by the calibration. The object under the illumination of the focused light spot will reflect light or emit fluorescence, which is coupled into the MMF and

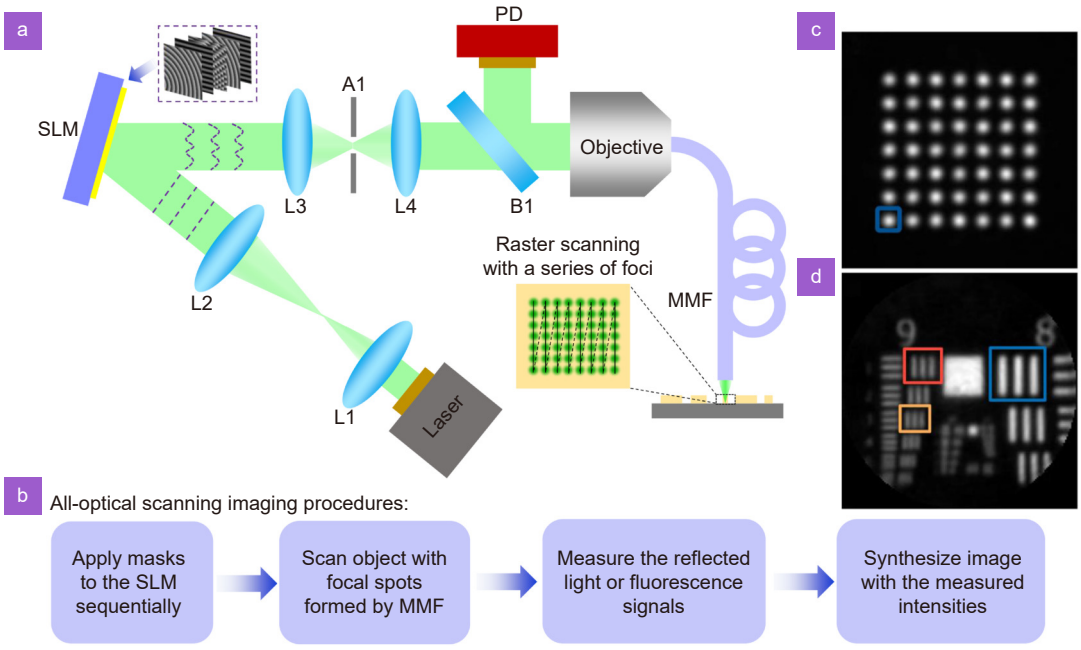

Fig. 6 | (**a**) Experimental setup of MFSE works in an all-optical scanning imaging manner. L1-L4: lens, A1: aperture, PD: photodetector, B1: beam splitter or dichroic mirror for reflected light or fluorescence, respectively. (**b**) Procedures to conduct all-optical scanning imaging, (**c**) combined image of sequentially generated focal spots at the distal end of MMF and (**d**) scanning imaging result of a test target. Figures (c) and (d) reproduced with permission from ref.[42], Springer Nature, under a Creative Commons Attribution 4.0 International License.

propagates in the opposite direction to the illumination light. To direct the signal light into the photodetector, a beam splitter or a dichroic mirror is arranged in the proximal end of the MMF for the reflection or fluorescence imaging modes, respectively.

The all-optical scanning imaging procedures are outlined in Fig. 6(b). The stored masks are sequentially loaded onto the SLM, allowing focal spots to be generated at different positions in a temporal sequence for scanning imaging. Generally, these sequentially generated focal spots are used to scan the sample in a raster scanning manner. Figure 6(c) presents a typical combined image of sequentially generated focal spots at the distal end of MMF. These sequentially generated focal spots are evenly distributed at the grid points of a square lattice to sample the object. Then, the image of an object is synthesized using the time-varying intensity signals measured with the photodetector along with the calibrated position data of the corresponding focal spots. As an example, the synthesized image of a resolution target is shown in Fig. 6(d).

From the above description, it is evident that the alteration of the focal spot's position in the MFSE is accomplished through a purely optical method, i.e. wavefront shaping with various masks applied in the SLM. All the imaging-assistive elements like the SLM are positioned at the proximal end of the MMF. Consequently, the footprints of MFSEs are solely determined by the diameters of MMFs, offering a notable advantage over the single-mode fiber scanning endoscope that relies on the mechanical actuator located at the distal end of the fiber to conduct scanning imaging. Due to the reduced probe size, the MFSE promises great potential for minimally invasive biomedical applications. Certainly, the single-mode fiber scanning endoscope, being a mature and well-established technology, also has notable advantages when compared to MFSEs, including strong resistance to external disturbance and faster scanning imaging speed. The issues with MFSEs in these two aspects are indeed major factors that hindered their widespread practical applications. In order to harness the potential of MFSEs in terms of small footprints, it is necessary to overcome these practical challenges.

Scanning imaging performance

As a promising imaging technique, the scanning imaging performance of the MFSE has garnered significant attention from researchers. Currently, the following performance factors are the primary concerns of the MFSE, including imaging resolution, imaging contrast, scanning imaging speed, stability of the system, working distance and FOV. Many strategies have been suggested to enhance these performance aspects. Below, we will provide an overview of these performance improvement strategies. Due to the fundamental constraint imposed by working distance and FOV on imaging resolution and contrast, the developments related to the working distance and FOV are not discussed in separate sections. Instead, they are involved in the discussion of imaging resolution and contrast in Sections *Imaging resolution* and *Imaging contrast*.

Imaging resolution

Imaging resolution determines how small objects can be distinguished by an imaging system. As a scanning imaging equipment, the imaging resolution of the MFSE is primarily determined by the sizes of focal spots, which are affected by factors stemming from both the experimental implementation and the fundamental physical principle. In the aspect of experimental implementation, the fidelity of the wavefront shaping mask acquired by a certain calibration technique is important. If the wavefront shaping mask cannot accurately compensate for the modal scrambling of the MMF, the focused light spot disperses and cannot achieve the minimum size. In the imaging process, whether the modulated optical field can be coupled into the MMF at the correct spatial position also has a significant impact on the focal spot. Nevertheless, these issues can be addressed by carefully arranging the experiments. As shown in Table 1, most focal spots reported in these representative works achieved a diffraction-limited size. Therefore, the more challenging factors that restrict the sizes of focal spots are imposed by fundamental physical principles, including the numerical aperture (NA) of the MMF probe and the working distance.

We first introduce the influence of NA on imaging resolution and the related advancements. MMFs with a larger NA can support the propagation of more eigenmodes and thereby provide more controllable degrees of freedom to produce smaller focused light spots. NAs of commonly available MMFs typically range from 0.2 to 0.5, which results in imaging resolutions achieved in most works being larger than 1 μm as displayed in Table 1. To further improve the imaging resolution, so far, several approaches have been proposed to increase the NA. In 2013, Choi et al. and Papadopoulos et al. found

that placing a highly scattering medium in front of an MMF can physically increase the NA of the entire imaging system. Choi et al. coated a layer of ZnO nanoparticles on the surface of the MMF and found that the effective NA of the system increased from 0.22 to 0.4[85]. Papadopoulos et al. employed a layer of 20 μm white paint deposited on a glass slide as the scattering medium. They found that the size of the focused light spot decreases with the increase of distance between the scattering medium and MMF[86]. When the light field is focused at 800 μm away from the scattering medium, the size of the focal spot remains smaller than 1 μm, exhibiting a significant improvement in both NA and working distance. The increased NA is attributed to both the enlargement of the physical output aperture and the enhancement of coupling from high- to low-order modes that can propagate through the MMF. However, the use of scattering media significantly increases the transmission loss and degrades the collection efficiency of the reflected signal. Jang et al. later adopted a holistic random encoding method to improve the signal-to-noise ratio of image reconstruction[87].

The other method to increase the NA is assembling micro-optic components on the facet of MMF. In 2013, Bianchi et al. fabricated a micro-parabolic reflector on the facet of MMF using the two-photon polymerization technique[88]. The NA of the obtained device is close to 1, and it can produce a focal spot with an FWHM of ~300 nm. Apart from these creative innovations, one of the most direct approaches to increasing NA is leveraging specialized optical fibers. In 2016, Amitonova et al. demonstrated that well-designed multimode photonic crystal fibers (PCF) possess an NA of ~0.6, which is larger than those of commonly available MMFs and thus enables the focal spot to have a subwavelength size[89]. However, these hollow PCFs are not well-suited for operation in the aqueous environment. Later, Leite et al. fabricated an all-solid soft-glass MMF that achieves an NA exceeding 1 for wavelengths below 620 nm and reaching 0.96 at 1064 nm[90], showcasing significant promise in enhancing imaging resolution.

Working distance is another fundamental factor limiting the sizes of focal spots and thus the imaging resolution. Working distance is the length between the focusing plane and the fiber facet. Given the fact that the aperture of a specific MMF is fixed, as the working distance increases, the maximum propagation angle of light rays that contribute to the focal spot is reduced, which means the effective NA of MMF exploited for light focusing is smaller than its intrinsic NA[70]. As the effective NA becomes smaller due to the increase in working distances, the sizes of focal spots inevitably increase. In some reported studies, long-distance three-dimensional (3D) scanning imaging using MMF has been achieved based on the time-of-flight technique and optimized phase modulation strategies. However, these techniques can only enhance the contrast of focal spots and the efficiency of collecting signals at long distances. The imaging resolutions in these works were significantly degraded to the millimeter scale[91,92]. The above-mentioned work that used a glass slide deposited with white paint as the scattering medium to increase the NA can simultaneously improve the imaging resolution and increase the working distance[86]. However, since a glass slide with a large aperture was required to be positioned at the distal end of the MMF, the most remarkable advantage of the MFSE, i.e. an ultrathin probe, is sacrificed. Therefore, the trade-off between working distance and imaging resolution is still a challenge in this field. In experiments, it is necessary to properly select the imaging plane to balance the imaging resolution and working distance.

Furthermore, it should be noted that the uniformity of produced focal spots at different raster-scanning positions is also a key factor affecting the overall imaging resolution. In some situations, the MMF can only achieve diffraction-limited focusing in the region near the core while the focal spot in the region closer to the cladding becomes elliptical[93]. Descloux et al. demonstrated that the number of modes required for diffraction-limited focusing in edge is much more than that required for central focusing[94]. Therefore, to achieve diffraction-limited focusing at the edge, the phase mask must be sufficiently complex to fully compensate for the mode dispersion, which implies that more divided segments on SLM are needed. They suggested that a minimum of $V^2/4$ (V is the normalized frequency of MMF) segments should be employed to ensure uniform raster-scanning imaging[94]. In case the segments of SLM are limited, Lyu et al. suggested coupling light closer to the core's edge to acquire a round focal spot for scanning imaging[93]. Besides, it was found the MMF with a square core can focus light more uniformly at different positions than the MMF with a round core. Therefore, this novel MMF is a competitive candidate to substitute the traditional MMF with a round core for scanning imaging[95]. Moreover, the computational algorithms based on convolution and

deconvolution are also choices to improve the image resolution[96].

The above-discussed methods are mainly focused on improving the imaging resolution by modifying the MMF probe or optimizing the experimental implementations. In addition, the integration of MMF with other advanced scanning imaging modalities, such as the confocal endoscopy and two-photon imaging modality can also enhance the imaging capacity[97–99]. We will introduce these advancements in Section *Different scanning imaging modalities* in detail.

Imaging contrast

Imaging contrast is another crucial parameter for an imaging system[100]. The scanning imaging process of MF-SE comprises two sequential steps: focusing the optical field to create an illumination spot on the sample and capturing the signal light reflected or emitted by the sample. Several factors have substantial impacts on the imaging contrast in both steps.

In the aspect of optical field focusing, the contrast of focal spots generated through an MMF is a determinant. As we have mentioned in Section *Principle of multimode optical fiber scanning endoscope*, the contrast of the focal spot is characterized using two metrics, i.e. the enhancement factor (η) and the power ratio (PR). According to calculations, if an MMF supports 1000 eigenmodes, the PR value of the generated focal spot can exceed 99%[101]. Therefore, the PR value of the focal spot obtained in experiments below this theoretical calculation is attributed to imperfect experimental implementation rather than physical limitations. To fully utilize the numerous eigenmodes of an MMF for light focusing, it is essential to ensure that the number of input modes controlled by the SLM is comparable with the number of eigenmodes, which has already been mentioned in the preceding analysis of the uniformity of focal spots. Within a certain range, the more input modes we can control, the higher the PR of the focal spot will be. However, as the number of input modes increases, the number of pixels contained in each segment partitioned on the SLM decreases inevitably, which may unexpectedly lead to the reduction of PR when LC-SLM is utilized. This reversal is the result of the severe scattering noise present within the LC-SLM. These scattering noises seriously degrade the fidelity of the phase mask when the intensity of each input mode is low, consequently diminishing the quality of the focal spot[102]. This issue is less pronounced with the use of a DMD, one of the reasons for its growing popularity.

When the controllable segments are enough, the other key point is to comprehensively perform complex modulation of the optical field, including phase, polarization, and amplitude. According to the analysis of Čižmár et al., lacking polarization and amplitude control may result in ~50% and ~21.5% of the available optical power being randomly dispersed across the output area as noise, respectively[23]. To control the two polarizations of light, the transmission matrices of both polarizations should be individually measured and the mask loaded onto the SLM is a superposition of masks designed for the independent modulation of each polarization. If only one polarization is controlled, the single circular polarization can yield better PR than the linear polarization. The amplitude modulation is achieved by manipulating the diffraction grating on the modulator to prevent the dominant noise-contributing modes from coupling into the fiber. However, this comes at the cost of reducing the overall output power. By optimizing the experimental setup and employing the complex modulation, Gomes et al. have achieved focal spots with a PR of ~96%, which is the highest value reported to date[84].

In addition to the two fundamental requirements, there are numerous experimental details that must be carefully considered in both the calibration and imaging procedures to achieve near-perfect focusing. In the process of calibration, different techniques involve various experimental setups and thus the origins of mask measurement errors vary. We have already clarified the key points for each calibration technique in Section *Principle of multimode optical fiber scanning endoscope*. In terms of the imaging process, Gomes et al. have comprehensively analyzed the important experimental details that may affect the focusing quality, such as the propagation angle and polarization of the incident light relative to the DMD, the wavefront aberration originating from the DMD curvature, and the ghost diffraction orders of DMD[84]. When all these issues in experiments are addressed properly, near-perfect focusing is possible. Moreover, Tučková et al. proposed two algorithms based on the regularized iterative inversion and the regularized direct pseudo-inversion to enhance the image contrast by post-processing the obtained image with the original intensity distribution of speckle-contaminated focal spots[101]. In case the number of controllable segments on the SLM is insufficient, Zhang et al. introduced a

wavelength modulation method to suppress background noise and thus improve the imaging contrast[103].

In the aspect of signal collection, the NA of MMF is the key factor influencing imaging contrast. Studies related to increasing the NA of MMFs can be found in Section *Imaging resolution*, where a detailed introduction has already been provided. In addition to these optimizations mentioned above for the most common MFSE system working in reflection mode or fluorescence imaging mode, it is also possible to combine this endoscope technique with other advanced imaging techniques, such as confocal and two-photon imaging, to further enhance the imaging contrast. Detailed explanations are provided in Section *Different scanning imaging modalities*.

Scanning imaging speed

As an endoscopic technique aims at biomedical applications, the imaging speed is one of the key metrics determining its practicality. Ideally, during the MMF scanning imaging process, there would be no need for repetitive calibrations. Instead, the wavefront reshaping masks recorded during the calibration stage for the generation of different focal spots would sequentially be transferred to the SLM to complete the all-optical scanning. Therefore, the imaging speed mainly depends on the refresh rate of the SLM and the communication speed between the SLM and the computer. So far, the mask transfer time between the computer and the SLM has been drastically reduced to negligible levels by utilizing a powerful modern Graphics Processing Unit (GPU)[2,104,105]. As such, the refresh rate of the SLM is currently the most critical factor limiting imaging speed.

In the early stage, LC-SLMs were widely employed owing to their excellent wavefront reshaping performance. However, the typical refresh rate of LC-SLMs is less than 200 Hz, which is too low to meet the imaging demands of moving objects. Pairing LC-SLMs with faster beam-steering devices, such as the acoustic-optic deflector and galvanometer mirrors, can markedly boost acquisition speed but considerably sacrifice the maximum pixel resolution[25]. Later, the DMD with a refresh rate exceeding 20 kHz became the favored optical field modulation device. Although DMD is a binary-amplitude modulation device, it can achieve complex modulation for both amplitude and phase using the Lee hologram method[43,46,106]. So far, the MFSE system employing a DMD as the SLM has achieved near video rate to observe the deep brain of living anesthetized mice (Fig. 7) and moving humans[42,107]. Besides, DMDs also exhibit higher wavefront reshaping fidelity compared with LC-SLMs because DMDs do not experience the strong scattering and flicker effect that LC-SLMs encounter[102,108]. Certainly, DMD has disadvantages, such as lower diffraction efficiency compared to LC-SLMs, rendering it unsuitable for applications requiring high intensity[108,109]. In summary, DMD currently is the optimal choice for MFSE from the perspective of imaging speed.

The above analysis is based on the ideal scenario where the MMF remains undisturbed during usage. However, in most practical applications, the movement or bending of the MMF is inevitable, which renders the previously calibrated mask ineffective. The relevant studies are introduced in next Section in detail. If frequent recalibration is necessary during usage, the imaging speed will be significantly reduced. How to further boost the imaging speed in this scenario remains a significant challenge for the MFSE system.

System stability

In practical use, the stability of the entire MFSE system is of utmost importance. However, both the MMF and auxiliary optical paths within the system are susceptible to external dynamic disturbances, leading to the instability of the imaging performance. The stability of the MFSE system is primarily assessed by comparing the system's transmission characteristics of light fields before and after external disturbances. Several different parameters, including normalized focus intensity, the correlation coefficient of the MMF speckles and the structural similarity index of obtained images, have been employed to quantitatively measure the system stability. When subjected to external disturbances, the quality of the focused light spot produced by MFSE may change, thereby affecting the scanning imaging performance. Caravaca-Aguirre et al. have used normalized focus intensity to evaluate the stability of the MFSE system under displacement disturbances[110]. Besides, MFSE typically generates speckle at the output end of the MMF. It is also feasible to measure the stability of the system by calculating the correlation coefficient of speckles generated before and after external disturbances under the same light field excitation[111–113]. Furthermore, the structural similarity index of scanning imaging results obtained in different conditions was also employed to evaluate the system stability[113,114]. Next, we will discuss the effects of environmental disturbances on the MMF and its auxiliary optical

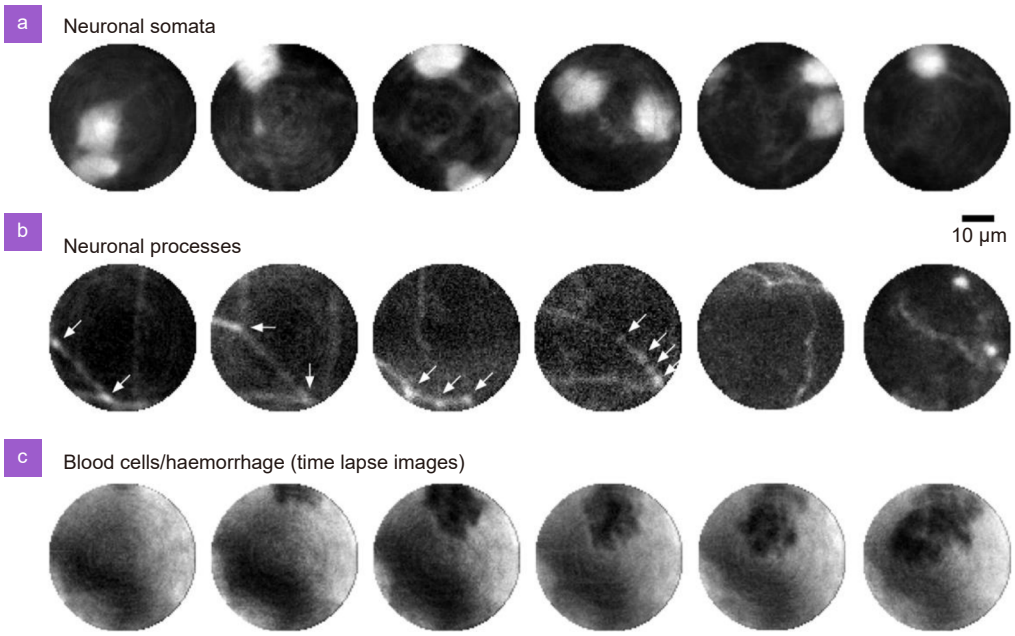

Fig. 7 | Images of (**a**) neuronal somata and (**b**) neuronal processes in the brain of a mouse, as well as (**c**) a haemorrhage in the primary visual cortex were captured by the MFSE in vivo with an imaging speed of 3.5 frames/s. Figure reproduced with permission from ref.[42], Springer Nature, under a Creative Commons Attribution 4.0 International License.

paths in imaging, along with the current solutions.

It is well known that the bending, twisting, and temperature changes of the MMF can significantly alter its modal properties, making the wavefront shaping masks obtained through the calibration process no longer suitable for achieving focus in the new condition. To overcome this challenge, there are currently two alternative strategies to consider. The first strategy is to shield the MMF from external disturbances or develop MMFs that are insensitive to disturbances. For example, Papadopoulos et al. encapsulated the MMF within a 25-gauge needle to prevent the bending of MMF as displayed in Fig. 8(a)[70]. However, this method considerably diminishes the benefits of MFSE in terms of flexibility and an ultrathin probe, which are preferred in many biomedical applications. In terms of the disturbance-insensitive fibers, graded-index MMFs are widely acknowledged to offer superior resistance to external disturbances compared to step-index MMFs. At a fundamental level, external disturbances affect the scanning imaging performance of MMFs by altering the mode propagation constants and inducing mode coupling. According to the mode-coupling theory, the mode-coupling coefficients of graded-index MMFs are significantly smaller than those of step-index MMFs[115]. As such, the external disturbances induced power coupling between modes in step-index MMFs is stronger than that in the graded-index MMFs. The weak mode coupling property of graded-index MMFs makes them more resistant to external disturbances[110]. Flaes et al. also experimentally demonstrated that the imaging performance of the graded-index MMF is indeed less affected by deformation when compared to step-index MMFs[116]. Moreover, they proved that the graded-index MMF featuring a precisely parabolic refractive index profile is highly resistant to the effect of bending. The bending deformations in such MMFs almost do not lead to mode coupling but are equivalent to slight fiber stretching. However, the fabrication of ultraprecise parabolic-index fibers is still a challenge. Further, Loterie et al. compared the propagation characteristics of different MMFs under the disturbance of bend translation and found that MMFs with small core sizes and large NAs are insensitive to such disturbance[117]. The bend in these MMFs can be translated up to 25 mm with negligible impact on the effectiveness of the original calibrated masks. While these intriguing findings enhance the operational flexibility of MMF to some extent, the demands for unrestricted manipulation of MMF in practical applications still present significant challenges.

The other strategy is to perform the real-time recalibration of the transmission matrix for MMFs. A certain progress in this aspect has been achieved through both theoretical and experimental approaches. In the

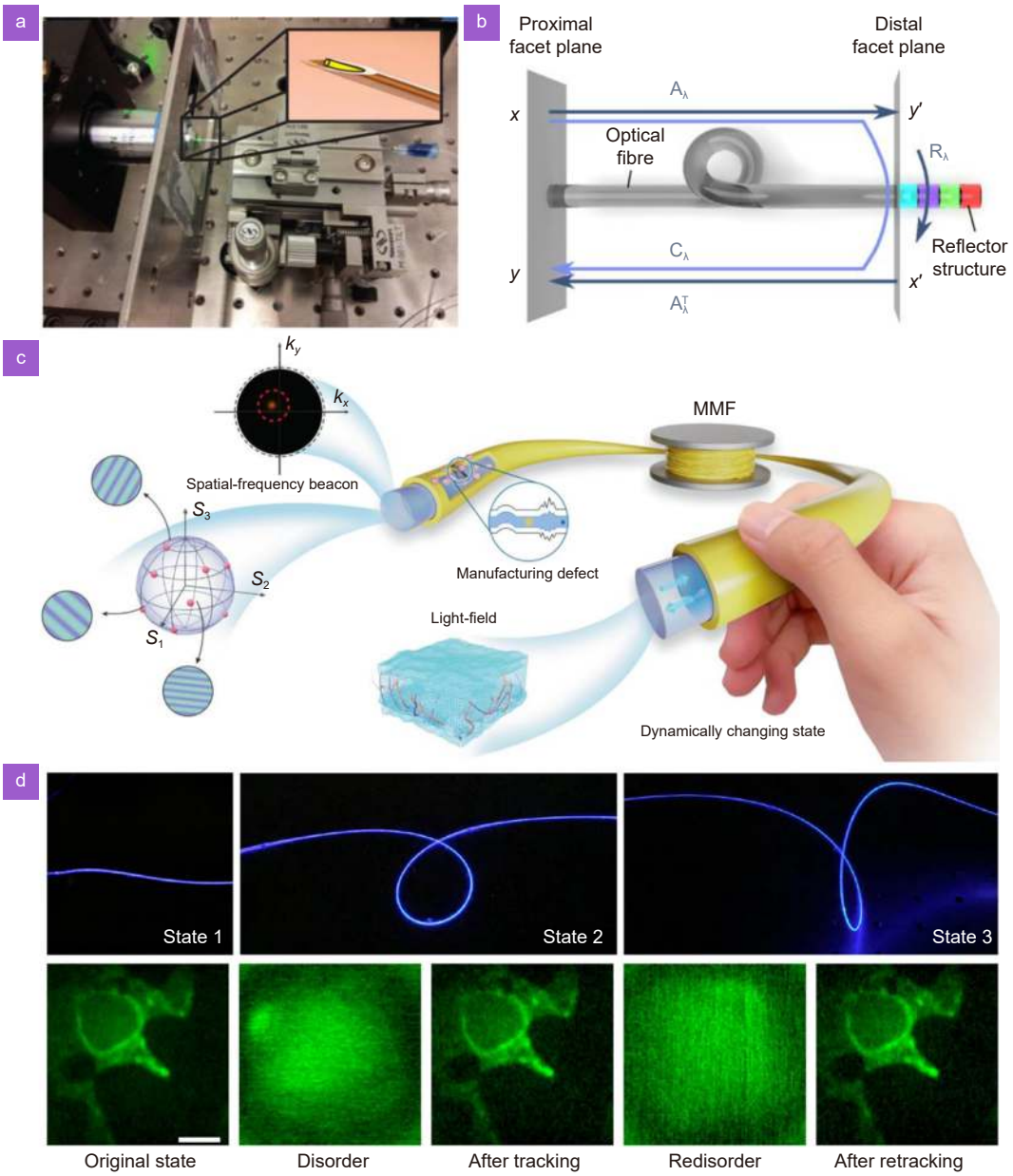

Fig. 8 | (**a**) The image of an MMF encapsulated within a 25-gauge needle to prevent the deformation of MMF. (**b**) Schematic to illustrate the calibration of the transmission matrix at the proximal end of MMF based on the reflection matrix scheme. A metasurface reflector is added at the distal end of MMF to facilitate the measurements of reflection matrices for different wavelengths. (**c**) Schematic of spatial-frequency tracking adaptive beacon light-field-encoded endoscopy to detect and track disorders caused by movements and manufacturing defects. (**d**) The geometric state change and the corresponding imaging recovery using the STABLE tracking method. Figure reproduced with permission from: (a) ref.[70], © Optica Publishing Group, (b) ref.[120], American Physical Society, under a Creative Commons Attribution 4.0 International License, (c) and (d) ref.[114], Springer Nature, under a Creative Commons Attribution 4.0 International License.

theoretical aspect, Plöschner et al. established a model that can accurately derive the transmission matrix of an MMF in a bending state from the transmission matrix of the same MMF in the straight state[61]. However, this method requires real-time knowledge of the geometric conformation of MMF and thus has substantial limitations in practical application. In terms of experiments, the key challenge is how to perform recalibration using information obtained solely from the proximal end of the MMF rather than the traditional method relying on the interferometric measurement at the distal end of MMF[24]. So far, several experimental schemes have been proposed to overcome this challenge. In 2013, Farahi et al. employed a beacon source to generate speckle patterns at the proximal end of the MMF, which can be used to identify the correct transmission matrix from the pre-

calibrated database for the current fiber conformation[118]. Later, schemes that involved utilizing the reflected light from the distal end of MMF to deduce its transmission matrix were presented[119–121]. As exemplified in Fig. 8(b), these schemes often require the fabrication of micro-optics components, such as partial reflectors and metasurfaces, at the distal end of the optical fiber to facilitate the measurement of the reflection matrix[119,120]. In 2021, the memory effect of MMFs was also exploited to estimate the transmission matrix at the proximal end of MMF with the assistance of a guide star placed at the distal end[52]. These techniques can achieve recalibration of the transmission matrix at the proximal end of MMFs, but some issues exist, such as slow calibration speed on the order of minutes, requirements of complex surface engineering, and limited applicable scenarios.

Recently, Wen et al. proposed a technique referred to spatial-frequency tracking adaptive beacon light-field-encoded (STABLE) endoscopy as illustrated in Fig. 8(c) to quickly recalibrate the transmission matrix[114]. The key point of this technique is forming spatial-frequency beacons at the Fourier plane of the proximal facet of MMFs with full-vector modulated incident wavefronts. By maximizing the intensity of the spatial-frequency beacon, the current fiber deformation state can be quickly determined, and the corresponding pre-calibrated transmission matrix can be sought for scanning imaging. The STABLE method achieved ~1 kHz disorder tracking frequency, ensuring stable imaging in long MMFs under fiber deformation and complex operating conditions as shown in Fig. 8(d). The STABLE method, to some extent, addressed the above-mentioned issues in other techniques, demonstrating a significant reduction in tracking time and eliminating the need for complex distal facet engineering requirements. Certainly, this method also has some restrictions on operation conditions, such as the length of MMF < 50 m, bending curvature < 80 m^{-1} and twisting angle < 130°. Although these restrictions have been significantly relaxed, exploring more versatile and powerful real-time calibration techniques is still of interest in this field.

In addition to the modal instability of MMF, the auxiliary optical paths also inevitably experience external disturbances, subsequently causing displacement, defocusing, and tilting between the incident light and the MMF. To address the mechanical and thermal drifts, many optimization procedures for the rapid calibration of the relative position between the optical path and MMF have been proposed[61,122]. Besides, the removal and reinsertion of MMF into the imaging system also lead to the change of relative position between the optical path and the MMF. This challenge has been overcome by Schmidt et al. using a customized headplate and the adaptive optics method[123]. Moreover, the thermal drift issue often occurs in the SLM because it needs to frequently update masks during scanning imaging. This problem can be solved by using a thermoelectric cooler to stabilize the temperature of the SLM[124]. Finally, fluctuations in environmental refractive index and temperature may also affect the imaging performance of MFSEs. The above-mentioned STABLE technique can achieve high-resolution imaging in this scenario as well. Besides, calibrating MMFs in a medium with a refractive index matching the target application environment is also a alternative solution[97]. Overall, these works have effectively promoted the stability of the auxiliary optical path in the MFSE system. The key efforts to enhance the stability of MFSE systems should remain centered on mitigating the impact of external disturbances in MMFs. Finally, to intuitively exhibit the scanning imaging performance of the existing systems, imaging performance factors reported in some typical works are summarized and presented in Table 2. The unique features of these work are also provided.

Different scanning imaging modalities

These works discussed in Section *Scanning imaging performance* to enhance the imaging performance of the MFSE system are suitable for the most common reflection and linear fluorescence imaging modalities. In fact, to achieve further enhancement in the overall imaging performance, other advanced imaging modalities working in the scanning imaging manner can also be integrated with the MFSE to leverage the advantages of different technologies. A prominent advantage of MFSE is its capability to access and image tissues deep inside the body with minimal invasion, whereas other imaging modalities can provide high imaging contrast, excellent optical sectioning ability, and so on. For example, if the confocal imaging technique is employed to modify the signal acquisition module of the MFSE system, the imaging contrast and resolution of the MFSE can be improved. So far, MFSE has been successfully integrated with various imaging modalities, including confocal endoscopy, two-photon imaging, Raman imaging, second harmonic imaging, and photoacoustic imaging. These integrations demonstrate the remarkable adaptability

Table 2 | Scanning imaging performance of some existing systems.

Refs	Imaging resolution	Imaging contrast	Scanning imaging speed	Working distance	Field-of-view	Features
ref.[86]	<1 μm	η=2000	—	800 μm	256 μm × 192 μm	Using a scattering medium to increase NA
ref.[88]	300 nm	—	Limited by refresh rate of LC-SLM	3.8 μm	~30 μm circular area	On-fiber micro-optics to increase NA
ref.[84]	~1.76 μm	PR=96% η=20000	Limited by refresh rate of DMD	—	—	Complex modulation
ref.[42]	~1.18 μm	PR=75% η=3100	3.5 fps for 7-kilopixel images	5–15 μm	50 μm circular area	Deep brain *in vivo* imaging
ref.[2]	~1.27 μm	—	2.4 s per 120×120-pixel frame	≤100 μm	50 μm circular area	*In vivo* fluorescent imaging of neurons
ref.[114]	250 nm	PR≥85 %	2.5 fps for 96 × 96-pixel images	≤200 μm	100 μm –170 μm circular area	High recalibration speed under disturbances

and versatility of MFSE. Next, we will introduce the research progress related to the integration of MFSE with these imaging modalities in detail.

Confocal endoscopy

Confocal microscopy is a widely used scanning imaging technique, which offers superior image contrast and axial resolution compared to conventional wide-field microscopy[100,125,126]. The excellent imaging performance of confocal microscopy is attributed to the spatial filtering effect of a pinhole introduced in front of the photodetector. The pinhole is arranged in a conjugate plane with respect to the focal plane of the lens system. When the light beam is reflected from the sample and reaches the pinhole, only the light signals originating from the focal volume of the sample can pass through, while stray light around the focal point and out-of-focus light are filtered out. It is not feasible to directly transplant the confocal microscope arrangement into the MFSE system because of the modal scrambling properties of MMFs. When the light signals originating from the focal point are gathered and transmitted through an MMF, they exhibit speckle-like profiles. Regarding these speckles, it is impossible to form a conjugate focal plane for spatial filtering using a conventional lens system.

To overcome this challenge and enable the confocal imaging modality of MFSE, in 2015, Loterie et al. presented a solution based on an ingenious experimental setup. The key point of this solution is to modulate the signal light returning from the MMF through an SLM with the same wavefront shaping mask that generates the current illumination focal spot at the distal end of the MMF[127]. In accordance with the reversibility of the wave equation, if the returning signal light originates from the current focal spot generated by the MMF, then after modulation through the SLM, the signal light is in phase-conjugation with the incident illumination light on the SLM and is also a plane wave. The modulated signal light, following transformation by a lens, is able to pass through the pinhole positioned in the optical path without obstruction. Conversely, when the returning light originating from the stray light is modulated by the current mask, it cannot be phase-conjugated to the illumination light and thus is filtered out by the subsequent pinhole in the optical path. As such, the flexible utilization of the SLM enables MFSE to enhance its scanning imaging performance following the principle of confocal imaging modality. The scanning imaging ability of the confocal MFSE and the common reflection-mode MFSE is compared by employing 30 μm and 2 mm pinholes. The 2 mm pinhole has a limited spatial filtering effect and thereby is used to represent the situation of reflection-mode MFSE. These imaging results indicate that when MFSE operates in a confocal modality, the imaging contrast and resolution are significantly improved.

In addition to the SLM-based experimental implementation of the confocal MFSE, in 2015, Loterie et al. proposed another approach based on the digital confocal principle to realize the confocal imaging modality of MFSE[99]. A brief outline of the process to implement the digital confocal method is as follows. Firstly, the complex optical field profile of the returning light output from the proximal end of the MMF is reconstructed using digital off-axis holography. Secondly, the reconstructed optical field is multiplied by the transmission matrix of the MMF to simulate the propagation of light within the MMF. This calculation allows us to reconstruct the optical field profile on the sample plane.

Thirdly, a digital pinhole mask is used to selectively preserve the optical field within a range around the focal spot. The range is determined by the size of the digital pinhole. The total energy of the optical field in the preserved region represents the intensity value of a pixel in the image. Repeating this process during the scanning imaging procedure allows for the synthesis of an enhanced image. In addition to the digital confocal method, another correlation method is also employed to enhance image quality. According to the reversibility of light propagation, if the returning light that originates from the focal spot propagates back through the MMF, it should lead to a similar optical field as the input. On the contrary, the optical field originating from the region beyond the focal spot should be uncorrelated with the input optical field due to the modal scrambling properties of MMF. As such, the intensity value of each pixel in an image can be obtained by calculating the correlation between the reconstructed optical field of the returning light and the original illumination light at the proximal end of the MMF. The experimental results demonstrated that both the digital confocal method and the correlation method can enhance image contrast and resolution. The correlation method has a lower computational cost while the digital confocal approach is more flexible in terms of image processing. Recently, Singh et al. demonstrated that using multiple virtual pinholes to process the reconstructed optical field on the sample plane can further improve the imaging contrast to surpass that achieved with a single digital pinhole scheme[128,129]. The integration of MFSE with confocal fluorescence imaging is also theoretically studied[130]. According to the theoretical studies, the integrated setup should employ two SLMs to modulate the illumination light and fluorescence, respectively. Since the spectrum of fluorescence is generally broad, the bandwidth of the SLM and the dispersion of the MMF are key issues that need to be solved. So far, there are no reported experimental implementations of the confocal fluorescence MFSE.

Overall, compared to the conventional reflective MFSE, hardware-based confocal MFSE provides enhanced image contrast and improved resolution while maintaining the same imaging speed. Owing to the spatial filtering function, the confocal MFSE is capable of 3D scanning imaging. The digital confocal MFSE also exhibits these enhancements, but due to the need for data processing, it has a slightly slower imaging speed. Besides, in the hardware-based confocal MFSE, aberrations induced by the curved SLM surface are automatically corrected because the light is modulated by the SLM twice. The digital confocal MFSE is flexible, while the hardware-based confocal MFSE also offers some unique advantages.

Two-photon imaging

The two-photon fluorescence imaging technique that relies on the nonlinear two-photon excitation effect forms a significant branch within the realm of conventional scanning microscopy[131]. Two-photon excitation is the process in which fluorescent molecules simultaneously absorb two photons with a longer wavelength than that required for single-photon excitation, leading to the electronic transition to an excited state and the subsequent fluorescence emission. The fluorescence signal intensity in the two-photon excitation is proportional to the square of the excitation light's amplitude. Therefore, if a focused light spot is used for two-photon fluorescence excitation, the fluorescence signal will be concentrated within a smaller volume than the focused spot itself, which can significantly improve the resolution and signal-to-noise ratio of fluorescence imaging. Besides, due to the longer excitation wavelength in two-photon imaging, this technique offers better penetration of biological tissues than single-photon fluorescence imaging[132]. Despite these advantages, the realization of highly efficient two-photon absorption requires high photon density conditions, which are usually achievable with the use of femtosecond pulsed lasers. To combine the two-photon imaging modality with MFSE, it is necessary to achieve the spatiotemporal focusing of the femtosecond pulse laser with broad spectra using the MMF. However, this task is challenging because the modal and chromatic dispersion of MMF can lead to a speckled spatial profile of the optical field and temporal pulse broadening[133,134]. The wavefront shaping schemes mentioned earlier are mainly designed for the monochromatic case. When it comes to focusing femtosecond pulse laser, additional measures are needed to deal with the complex dispersion issues within the MMF.

In 2015, Morales-Delgado et al. proposed a time-gated digital phase conjugation scheme to focus the femtosecond laser through the MMF[135]. In the calibration, they used time-gated interferometry and off-axis holography to record the complex optical field of the laser pulse output from an MMF. The recorded information enables them to selectively reconstruct the phase-conjugated optical field corresponding to a set of modes with similar

group velocities. When the reconstructed optical field is coupled into the MMF, only the selected set of modes with negligible modal dispersion is excited in the MMF. These modes can generate a focal spot with minimal temporal broadening in the distal end of MMF. The quality of the generated focal spot is not high due to the utilization of only a portion of the eigenmodes. Since graded-index MMFs have a greater number of eigenmodes with similar group velocities, they are a superior choice for two-photon imaging compared to step-index MMFs. In the same year, they demonstrated that the focal spots generated with this method can be exploited for two-photon scanning imaging[136]. In the experiment, they use an additional prism pair to compensate for the group velocity dispersion. The time-gated mode selection method, in conjunction with this dispersion compensation measure, achieved the transmission and focusing of nearly Fourier-limited optical pulses. The output pulse has a duration of 120 fs, which is close to the initial pulse duration 100 fs. The two-photon scanning imaging experiment utilizing these focused laser pulses achieves ~1 μm and ~15 μm lateral and axial resolutions, respectively, which are smaller than the resolution of single-photon fluorescence imaging. They also conducted the scanning imaging experiment within a 3D volume to demonstrate the depth sectioning ability of the two-photon MFSE, which is a significant advantage of the two-photon MFSE compared to the linear fluorescence imaging modality of the MFSE.

Later, Pikálek et al. systematically investigated the impact of the bandwidth of both SLM and MMF on the focusing capability. Two dispersion compensation schemes, including the SLM correction and the prism correction, were provided to maximize the system's bandwidth[137,138]. When a continuous laser with the same wavelength as the central wavelength of the femtosecond pulse is used for calibrating the wavefront shaping mask, it is also possible to achieve the focusing of the femtosecond pulse without strict dispersion management. Compared to the previously mentioned approach, the quality of the focal spot obtained here is lower and the pulse duration is longer. Turcotte et al. demonstrated that focal spots produced by this approach can also be used for volumetric two-photon fluorescence imaging in living brain tissue[139]. Furthermore, Sivankutty et al. proved that when extremely short MMFs, typically spanning just a few centimeters, were used in the MFSE, the effects of dispersion on pulse broadening and femtosecond laser focusing can be safely neglected[140]. In such scenarios, the MMF can be directly applied to two-photon imaging without the specialized dispersion management.

In addition to the wavefront shaping method, in 2021, Velsink et al. also proposed a scheme based on the temporal shaping of pulses to achieve the two-photon MFSE[141]. When the femtosecond pulse is shaped in the temporal domain, the pulse duration is only short in a predefined area of the distal end of MMF, while the pulses in the other region are broadened. This enables enhanced two-photon excitation only in a predefined region. They achieved two-photon raster scanning imaging in a square-core step-index MMF using this method. Furthermore, considering the complex measures required to address dispersion issues in two-photon imaging, Laporte et al. suggested an alternative nonlinear imaging method, namely saturated excitation, to improve the fluorescence imaging resolution of MFSE[98]. The saturated excitation method only requires a narrowband continuous laser, which helps to avoid dispersion issues. Experimental results have shown that the resolution of MFSE based on saturated excitation is enhanced by 1.6 times in all three dimensions compared to the linear fluorescence imaging modality of the MFSE.

Overall, the current two-photon MFSE is not yet mature, and some pressing issues need to be addressed. On the one hand, the quality of the focal spots obtained with these mentioned schemes is relatively poor. As a result, the resolution advantage of two-photon imaging is partially offset by the relatively poor focusing quality. On the other hand, to achieve relatively high excitation power, an LC-SLM with high diffraction efficiency was necessary for wavefront shaping. However, this resulted in slow imaging speed. Therefore, the further advancement of the two-photon MFSE necessitates overcoming these challenges.

Raman imaging

Raman scattering is an inelastic scattering process that occurs when photons interact with molecules in matter. During this process, photons can either lose or gain vibrational energy from the molecules, resulting in a shift of the photons' wavelength toward longer or shorter wavelengths, which are well known as the Stokes shifts and anti-Stokes shifts, respectively. These wavelength shifts are associated with the vibrational transitions of chemical bonds within molecules. Therefore, Raman

scattering spectra can be used to identify chemical compounds, which finds extensive applications in pharmaceutical analysis, biological process detection, disease diagnosis and so on. Fiber probes are crucial tools for Raman spectroscopic imaging. The miniaturization of probes enables many new applications and has been an ongoing focus for researchers. With the advancement of MFSE, MMFs have rapidly emerged as highly promising candidates for Raman imaging probes due to their extremely small footprint. So far, both the spontaneous Raman scattering imaging and the coherent anti-Stokes Raman scattering (CARS) imaging techniques have been combined with the MFSE to achieve label-free endoscopic imaging with high chemical contrast.

In 2017, Gusachenko et al. first employed MFSE for Raman spectroscopic imaging by replacing the photodetector in the common reflection imaging modality with the spectral measurement module as shown in Fig. 9(a)[142]. A continuous laser with 532 nm wavelength was focused by the MMF as the excitation beam to induce Raman scattering on the sample pixel-by-pixel. The spectra measured at each pixel are a result of the superposition of Raman scattering spectra from different compounds. Therefore, they utilized a non-negative matrix factorization method to decompose the acquired spectral data and calculate the contribution weights of each compound to the overall spectrum. Then, the weight values of compounds at each pixel serve as the intensity of the image to generate the final Raman spectral image. To display the distribution of different compounds within the same image, several color channels are typically used to represent distinct compounds. Figure 9(b) displays the spectral components decomposed for four different pharmaceuticals. These pharmaceuticals cannot be distinguished in the bright-field image while their distributions can be well identified in the Raman image with chemical contrast as shown in Fig. 9(c). This result demonstrates the unique advantages of MFSE working in Raman imaging modality over other imaging modalities in compound analysis. Besides, theoretical analysis indicates that the light-focusing ability of MMF probes based on the wavefront shaping technique enhances Raman detection signal-to-noise ratio by more than three orders of magnitude compared to speckle illumination. Later, the Raman imaging MFSE was also exploited to acquire the distribution of compounds in optically cleared samples[143].

Despite the substantial potential of Raman imaging with MFSE, it has suffered from a strong Raman background noise from the silica material of MMF and extremely slow imaging speed. The background signal originating from the silica MMF covers a wide wavenumber range (<500–1700 cm^{-1}), which corresponds to the Raman shifts of many substances that need to be identified in clinical applications. To solve this problem, Deng et al. proposed using a sapphire MMF as a substitute for the silica MMF in Raman imaging[144]. The sapphire MMF itself only has several sharp Raman peaks and thereby allows highly efficient detection and imaging in a wavenumber range of >800 cm^{-1}. However, this solution is imperfect because sapphire MMFs lack cladding, causing their optical transmission properties to fluctuate with environmental changes and thus resulting in a degradation of scanning imaging performance. In terms of the slow imaging speed, it is primarily constrained by the extremely weak spontaneous Raman signals, requiring a spectrometer with typically several seconds to acquire data from a single scanning point. Coherent anti-Stokes Raman scattering (CARS) is an effective approach to enhance the Raman signal and thereby significantly reduce the signal acquisition time[145]. In 2019, Trägårdh et al. successfully implemented the CARS imaging through the MFSE and achieved ~1 ms integration time for Raman signal acquisition in the epi-detection condition, which is several orders faster than the spontaneous Raman imaging[146]. In the experiment, two synchronized pump and Stokes pulses, after wavefront shaping by the same SLM, were focused onto the sample using the MMF. To acquire different Raman shifts, the wavelength of the pump laser should be tuned in a range. The use of laser pulse and tuning wavelengths of the pump beam both pose dispersion issues, which were solved by properly selecting graded-index MMF and calibrating the signal with the corresponding intensities of focal spots. However, when the graded-index MMF is used for CARS imaging, an unwanted four-wave mixing background signal exists due to the self-imaging of the focal spot inside the graded-index MMF. In 2022, Pikálek et al. presented an MMF probe made by splicing a segment of step-index MMF onto the graded-index MMF[147]. This special probe can prevent the focal point from forming inside the graded-index MMF, thereby significantly reducing the four-wave mixing background and improving the imaging contrast. Furthermore, another nonlinear imaging modality, i.e. the second harmonic imaging, has also been integrated with MFSE. In 2021, Cifuentes et al.

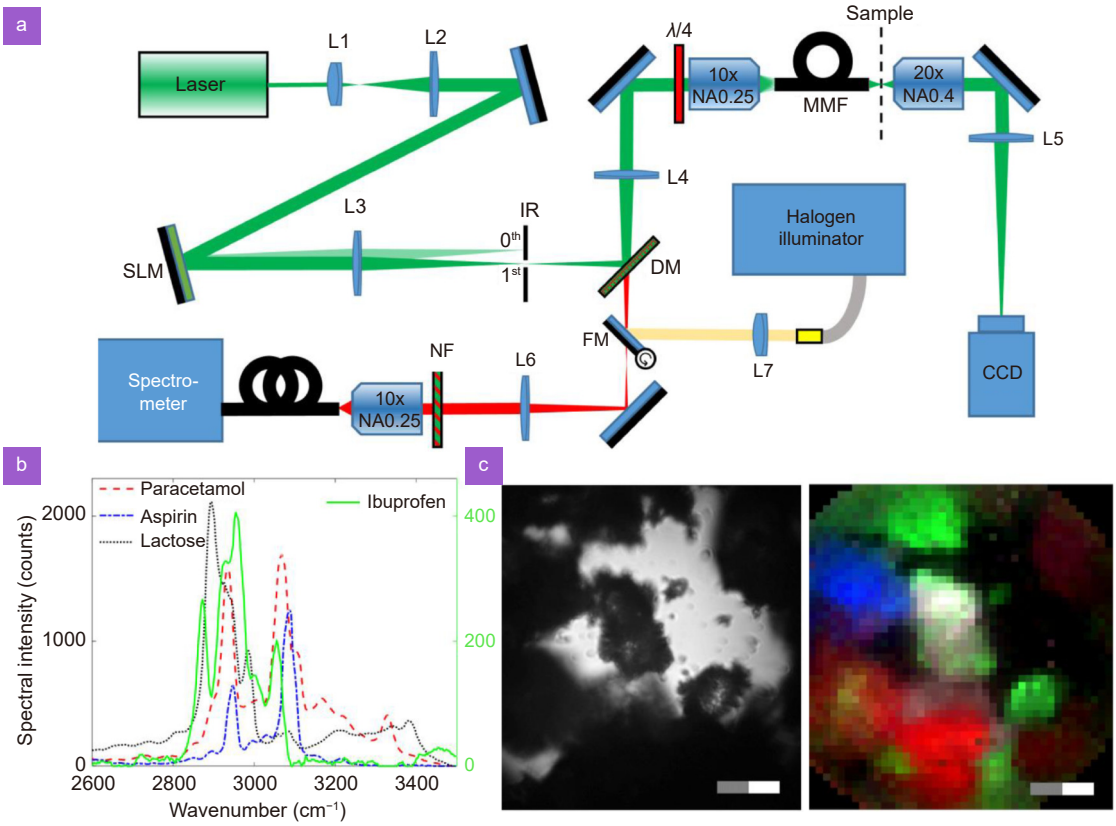

Fig. 9 | (**a**) Experimental setup of Raman spectroscopic imaging with the MFSE. (**b**) Raman spectral components of four pharmaceuticals. (**c**) Images of drug clusters obtained by bright field (left) and Raman spectroscopic (right) imaging modes. Figure reproduced from ref.[142], under the terms of the Creative Commons Attribution 4.0 License, Optica Publication Group. Some cropping adjustments have been made to the original image.

implemented polarization-resolved second harmonic imaging through MFSE with the same epi-detection manner[148]. By utilizing this imaging modality, they successfully discerned structural proteins deep within the mouse tail tendon and heart tissue. Both the Raman imaging and second harmonic imaging modalities are label-free techniques, which are important complements to fluorescence-based imaging methods. The successful implementation of the two imaging modalities with the MFSE greatly expands its versatility.

Photoacoustic endoscopy

Photoacoustic imaging is a widely used hybrid imaging modality[149], which merges the principles and advantages of optical excitation and ultrasound detection to achieve high-resolution images of objects. In photoacoustic imaging technique, a nanosecond pulse laser with a wavelength in the high absorption band of the sample is used for illumination. The temperature of the region illuminated by the pulse laser changes, leading to the generation of acoustic signals based on the thermoelastic effect. These acoustic signals can be detected by ultrasound sensors and used to create images. Photoacoustic imaging based on the optical absorption effect can be carried out either in a label-free manner or with the addition of exogenous agents to enhance contrast. Besides, the photoacoustic imaging modality allows for 3D imaging through acoustic sectioning using time-resolved acoustic signals or optical sectioning with focal spots at varying depths. Nevertheless, the two sectioning approaches both have limited depth of penetration. To diagnose lesions deep within tissues or tubular organs, photoacoustic endoscopy with miniaturized probes is a favored solution.

It is clear that the MFSE using an ultrathin MMF probe and the photoacoustic imaging technique are mutually compatible and offer complementary advantages. Recently, some researchers have combined these two techniques to achieve photoacoustic MFSE. In 2020, Mezil et al. implemented the photoacoustic MFSE by placing a fiber-optic ultrasound sensor with the MMF probe side-by-side[150]. The ultrasound sensor consists of a

single-mode fiber with a plano-concave polymer microresonator on its tip. In experiments, a nanosecond pulse laser was modulated by an LC-SLM using the masks obtained by the transmission matrix measurement method. Then, focal spots at different positions are sequentially produced and raster-scanned over a sample at the distal end of the MMF. The ultrasound signals acquired at each scanning point can be used to reconstruct the image. The lateral resolution of photoacoustic MFSE depends on the size of focused light spots and thus can be very small. However, due to the use of an LC-SLM for wavefront shaping, the imaging speed of their system was very slow. In 2022, Zhao et al. achieved a video-rate photoacoustic MFSE using a DMD as the SLM[151]. Masks employed for wavefront shaping were acquired by a real-valued intensity transmission matrix algorithm. The imaging speed and spatial resolution of this setup varied from ~2 to 57 frames per second and from 1.7 to 3 μm, which were determined by the scanning step size. This work employed a transmission detection manner with a bulky ultrasound detector, which hindered its practical usage. In the same year, they modified their setup by integrating a highly sensitive fiber-optic microresonator ultrasound sensor with the MMF probe within a 20 gauge medical needle while retaining the DMD for high-speed wavefront shaping[152]. In another work, they integrated a transparent ultrasound sensor based on an ITO-coated PVDF thin film on the distal end of MMF[153]. They also demonstrated the 3D imaging ability of the photoacoustic MFSE by both acoustic and optical sectioning. The axial resolution of optical sectioning is ~25 μm, which is almost half smaller than that of acoustic sectioning. As a scanning imaging technique, the single-frame imaging time of the photoacoustic MFSE depends on the scanning speed and the number of scanning points included in an image. When the scanning speed is constrained by the refresh rate of SLM, reducing the pixel number in an image is a necessary approach to boost imaging speed. To reduce the number of scanning points without compromising image resolution, Zhao et al. introduced a method that utilizes a deep convolutional neural network to reconstruct the high-resolution image from the sparse-sampled photoacoustic imaging result[154]. They validated that this method can boost imaging speed by 16 times without substantial degradation of image quality.

Finally, to intuitively compare the different imaging modalities of MFSE, the contents of some representative works studying these imaging modalities are summarized in Table 3. In terms of the experimental setups, different imaging modalities have varied requirements for light sources, detectors, and SLMs. The nonlinear imaging modalities, including two-photon imaging, spontaneous Raman imaging and CARS imaging, commonly require high peak intensity and total power for excitation, and thus the ultrashort pulse laser and the LC-SLM with high diffraction efficiency are employed. The slow imaging speed is a common problem for these imaging modalities due to the usage of LC-SLM. The long signal acquisition time of spontaneous Raman imaging is the dominant factor for its slow imaging speed. To note, the problems listed in the table only outline issues related to employing MMFs across different modalities rather than the inherent characteristics of the modalities. In another aspect, the confocal, two-photon and photoacoustic imaging modalities of MFSE all have been demonstrated to possess 3D imaging capacity, while the Raman and CARS imaging modalities can identify chemical compounds. Therefore, diverse imaging modalities greatly expand the application scenarios of the MFSE, which are difficult for the common reflection or fluorescence imaging mode of the MFSE. Notably, as these MMF-based imaging modalities are still in the developmental stage, applications presented in the literature are mainly focused on ex vivo imaging of samples. To promote the practical applications of these MMF-based imaging methods, significant efforts are still required to address the issues listed in the table.

Applications

Over the past decade, significant progress has been made in improving the MFSE system. However, we have to acknowledge that this technique is still in development and is not yet operational in practical applications. Nevertheless, some studies have begun to attempt the implementation of this technology in practical settings. Besides, many research works that aimed at improving the imaging performance of the MFSE and expanding its imaging modalities have included some application demonstrations. Next, we will provide an introduction to these application demonstrations of MFSEs, which mainly include biomedical imaging, 3D volume imaging and compound composition analysis.

Biomedical imaging is the primary target application field of MFSEs. The greatest advantage of MFSEs lies in their extremely small footprints, which promise minimal

Table 3 | Comparison of different imaging modalities of MFSE.

Modalities	Setup details	Resolutions	Imaging samples	Problems
Confocal endoscopy[127]	*NA*: 0.22; Pinhole: 30 μm; *P*: Photodiode; LC-SLM	R_l:1.3 μm R_a:14.9 μm	Cover glass, *ex vivo* human epithelial cells, polystyrene beads	Complex alignment
Two-photon imaging[136]	*NA*: 0.29; *S*: 800 nm fs-laser; *P*: PMT; LC-SLM	R_l:1 μm R_a:15 μm	Fluorescent red beads suspended in a PDMS	Dispersion management, poor focusing quality
Raman imaging[142]	*NA*: 0.22; *S*: 532 nm laser; *P*: Spectrometer	Spectral resolution 25 cm^{-1}-32 cm^{-1}	Polystyrene beads, aspirin, M. smegmatis, paracetamol, ibuprofen, L. robusta	Raman background noise of silica material
CARS imaging[146]	*NA*: 0.29; *S*: 661–668 nm (pump), ~830 nm (SK) ps-laser; *P*: PMT; LC-SLM	2 μm beads were discerned	Polystyrene beads, PMMA beads	Dispersion management, FWM noise
PA endoscopy[152]	*NA*: 0.29; *S*: 532 nm ns-laser; *P*: FOUS; DMD	R_l:1.2-1.4 μm; R_a:25 μm (O) and 50μm (A)	Mouse blood smear, carbon fiber phantom, standard resolution target	—

PA: photoacoustic; *NA*: numerical aperture of MMF; *P*: detector; *S*: light source; SK: CARS Stokes beam; PMT: photomultiplier tube; FOUS: fiber-optic ultrasound sensor; R_l and R_a are the lateral and axial resolution, respectively; O: optical sectioning; A: acoustic sectioning; FWM: four-wave mixing.

invasion in biological tissue during imaging. Besides, MFSEs can achieve endoscopic imaging for narrow tubular structures that cannot be accessed by the other endoscopes. In the early stages, biomedical imaging demonstrations primarily focused on some ex vivo cellular specimens, such as stained neuronal cells, human epithelial cells, CHO cells, and mouse red blood cells[70,99,140,152]. With the improvement in imaging speed, researchers began conducting in vivo imaging of live cells. In 2018, Ohayon et al. employed the MFSE to capture the processes of baby hamster kidney cells expressing GFP and rapid neuronal dynamics in vivo[155]. Subsequently, Turtaev et al. and Vasquez-Lopez et al. performed in vivo endoscopic imaging experiments on live animals using anaesthetized mice[2,42]. They utilized MFSE to observe subcellular neuronal structures, dendrites, and synapses in the deep layers of the mouse brain, while also monitoring the stimulus-driven Ca^{2+} responses in neurons. In addition to imaging the deep brain tissues with strong scattering characteristics, Wen et al. performed in vivo endoscopic imaging of tubular organs of animals, including the sheep's small intestine and pig esophagus[114]. They also conducted endoscopic imaging in lived mice and performed disease diagnosis on their colon tissues. In medical applications, endoscopes not only aid in the diagnosis of diseases but also can guide surgical interventions for treatment. Kakkava et al. have employed the two-photon MFSE to guide femtosecond laser ablation in biological samples for highly selective modifications, which demonstrates the potential applications of MFSE in assisting medical surgeries[156]. In biomedical imaging, the crucial technical parameters include imaging speed and the stability of the system. Some technological improvements, such as the use of DMD and STABLE technique, have elevated these two parameters, consequently enabling MFSEs to achieve the above advancements in biomedical imaging applications.

As a scanning imaging technique, MFSE can easily extend from two-dimensional imaging to 3D imaging scenarios. Even with common bright-field or fluorescence imaging modalities, 3D imaging can also be achieved by focusing the light field at various positions in the 3D space. So far, 3D volume imaging has been demonstrated not only in fluorescence microsphere samples but also in live animal models[114,122,157]. For example, Stibůrek et al. utilized the MFSE to conduct in-vivo volumetric imaging of the mouse brain and recorded the volumetric data of sub-cellular structures' dynamics[157]. In 3D imaging applications, a crucial technical parameter is the axial resolution. If MFSE adopts confocal and two-photon imaging modalities, the axial resolution can be significantly improved as we have discussed in Sections *Confocal endoscopy* and *Two-photon imaging*[99,140]. Moreover, when performing the volumetric imaging of tissues with strong optical scattering, imaging depth is also a crucial parameter. In such cases, the photoacoustic imaging modality of MFSE is preferred because its acoustic sectioning function can increase the imaging depth[152].

Furthermore, MFSE also can be used for composition

analysis of chemical compounds or biological substances by employing Raman imaging modalities, CARS imaging modalities, and second harmonic generation imaging modalities. For example, Gusachenko et al. demonstrated using Raman imaging modalities of MFSE to identify the spatial distribution of different pharmaceuticals in samples[142]. Cifuentes et al. successfully employed the polarization-resolved second harmonic generation imaging modality of MFSE to characterize different structural proteins in the mouse tail tendon and heart tissue[148]. Since these imaging modalities are label-free imaging techniques based on optical nonlinear effects, the focused light pulses generated by the MMF must have sufficient peak power to obtain strong imaging signals. Therefore, effective dispersion management is crucial in these applications.

Challenge and outlook

Although there have been significant advancements in improving the scanning imaging performance and expanding application fields of the MFSE, this imaging technology still encounters several daunting challenges. Here, we do not refer to challenges only faced by a specific imaging modality of MFSE, such as the dispersion issue in two-photon imaging, which have been introduced in the corresponding sections. Conversely, some common issues faced by MFSE across various imaging modalities are discussed, along with the potential remedies. From our perspective, four primary problems need to be addressed.

The first problem is the well-known modal instability of MMF under dynamic disturbances, such as the distortion and bending of MMF, mechanical stress, temperature fluctuation, etc. In Section *System stability*, we have reviewed the progress made by researchers in tackling this issue, which mainly involves developing MMFs with better disturbance-resistant ability, recalibrating transmission matrices by theoretical methods, and real-time recalibrating transmission matrices at the proximal end of MMF. However, these methods all have one or more of the following limitations: (i) stringent application conditions, (ii) slow processing speed, (iii) unsuitability for implementation during the in-situ imaging process, and (iv) involving complex engineering requirements and resulting in inadequate experimental resolution. The current state-of-the-art recalibration solution, while overcoming most of the aforementioned issues, still imposes a few restrictions on operation conditions[114]. Therefore, exploring more versatile and powerful approaches to promote the stability of MFSE is still of interest in this field. From our perspective, the most elegant solution is to start at the optical fiber device level and manufacture optical fibers that are extremely insensitive to disturbances. For example, we can develop ultraprecise parabolic-index optical fibers or modified disordered optical fibers taking advantage of the Anderson localization effect for robust image transmission[116,158]. Alternatively, we may need to synergistically combine different disturbance-resistant strategies to provide a robust imaging method that allows flexible MMFs to be used.

The second problem is the relatively slow imaging speed to acquire high-resolution images. As an imaging technique based on the point-scanning principle, the imaging resolution of MFSE is constrained by the size of the focal spot and the number of scanning points used to form an image. To achieve high image resolution, a large number of scanning points is required, which results in a reduction in imaging speed. Even if the currently available SLM with the fastest refresh rate is employed for wavefront shaping, the point-scanning speed is only ~23 kHz, which corresponds to a slow frame rate of ~2.3 fps (100×100 pixels). This outcome still falls short of the requirements for video-rate endoscopic imaging. Given the current hardware constraints, reducing the number of scanning points is essential to boost imaging speed. Certainly, we may sacrifice the FOV to simultaneously reduce the number of scanning points and maintain high imaging resolution. However, a large FOV is also very important for many applications. Another potential solution is to train a machine learning model to reconstruct the high-resolution image from the low-sampled image created with only a few scanning points[159,160]. This approach holds promise in simultaneously achieving fast imaging speed, high resolution, and a large FOV. The reliability and generalization ability of machine learning models are aspects that require in-depth study in this scheme. Notably, medical endoscopic imaging is one of the potential application areas of MFSE, where the imaging targets are relatively fixed for the diagnosis of a specific disease. Therefore, the demands on the generalization ability of machine learning models are not very stringent in this scenario. As such, machine learning solutions hold significant promise to promote the imaging speed of the MFSE.

The third challenge involves the trade-off between the

working distance and imaging resolution. This is a fundamental limitation determined by the aperture sizes of MMFs. As we have discussed in Section *Imaging resolution*, so far, there are still no effective approaches to simultaneously achieve excellent imaging resolution and long working distances[91,92]. Hence, it is necessary to introduce some new technologies, such as machine learning and synthetic aperture techniques, to overcome this challenge according to concrete application scenarios.

The last challenge, but also a prospect, is how to develop a miniaturized and integrated MFSE system to enhance the system's stability. The current optical configuration of MFSE is very complex. Especially, when full modulations on phase, amplitude and polarization of optical field are carried out to achieve high-quality focal spots, a large number of optical components are employed and all of them need to be precisely aligned. This sophisticated bulk optical setup is inherently challenging to be isolated from external disturbances, thereby leading to potential misalignment issues among myriad optical elements as we have reviewed in Section *System stability*. In the commercialization of products, it is not feasible to expect customers to master complicated system alignment methods proposed by researchers in the literature. In this scenario, a potential solution is to develop a miniaturized and integrated optical system for MFSE using photonic integrated chips. The wavefront shaping function, which is a key challenge of this idea, may be achieved through the combination of dense array waveguides, phase shifters, and optical steering techniques. Anyway, the feasibility of this scheme requires collaborative validation from experts in different research fields.

Conclusions

MFSE is a highly promising endoscopic imaging system that has the potential to replace single-mode fiber and fiber bundle endoscopes due to its ultrathin footprint and high information transmission density. Over the past decades, MFSE has attracted extensive research interest and achieved substantial advancements in improving imaging performance and extending its applications. In this review, we first introduced the wavefront shaping principle to generate focal spots through MMF and procedures to implement all-optical scanning imaging without using mechanical actuators. Developments of three techniques, including transmission matrix measurement method, digital phase conjugation method and phase optimization algorithms, to acquire the mask for wavefront shaping with the SLM are reviewed in detail. Then, we focus on the scanning imaging performance of MFSE and strategies employed to enhance these performance metrics. In addition to some versatile improvements, combinations of some advanced imaging modalities, including confocal endoscopy, two-photon imaging, Raman imaging, and photoacoustic imaging modalities, with the MFSE systems to enhance the imaging performance for specific application scenarios are also presented. The applications of MFSEs that have been demonstrated in literature are introduced. Finally, we summarize the challenges faced by the current MFSE and the potential solutions. Looking forward to the future, if the mentioned problems in the current MFSE system can be overcome, MFSE could initiate its journey toward commercialization. Owing to certain trade-offs among various imaging performance metrics, it is possible to optimize the most crucial performance indicators based on specific application scenarios. The successful commercialization of MFSE is certain to substantially drive the progress of diverse application fields spanning biology, medicine, and industry.

References

1. Litynski GS. Endoscopic surgery: the history, the pioneers. *World J Surg* **23**, 745–753 (1999).
2. Vasquez-Lopez SA, Turcotte R, Koren V et al. Subcellular spatial resolution achieved for deep-brain imaging in vivo using a minimally invasive multimode fiber. *Light Sci Appl* **7**, 110 (2018).
3. Gaab MR. Instrumentation: endoscopes and equipment. *World Neurosurg* **79**, S14.e11–S14.e21 (2013).
4. Liu HH, Hu DJJ, Sun QZ et al. Specialty optical fibers for advanced sensing applications. *Opto-Electron Sci* **2**, 220025 (2023).
5. Jiang BQ, Hou YG, Wu JX et al. In-fiber photoelectric device based on graphene-coated tilted fiber grating. *Opto-Electron Sci* **2**, 230012 (2023).
6. Hopkins HH, Kapany NS. A flexible fibrescope, using static scanning. *Nature* **173**, 39–41 (1954).
7. Hopkins HH, Kapany NS. Transparent fibres for the transmission of optical images. *Opt Acta Int J Opt* **1**, 164–170 (1955).
8. Kao KC, Hockham GA. Dielectric-fibre surface waveguides for optical frequencies. *Proc Inst Electr Eng* **113**, 1151–1158 (1966).
9. Sun JW, Wu JC, Wu S et al. Quantitative phase imaging through an ultra-thin lensless fiber endoscope. *Light Sci Appl* **11**, 204 (2022).
10. Orth A, Ploschner M, Wilson E et al. Optical fiber bundles: ultra-slim light field imaging probes. *Sci Adv* **5**, eaav1555 (2019).
11. Pan YT, Xie HK, Fedder GK. Endoscopic optical coherence tomography based on a microelectromechanical mirror. *Opt Lett* **26**, 1966–1968 (2001).
12. Smithwick QYJ, Seibel EJ, Reinhall PG et al. Control aspects

of the single-fiber scanning endoscope. *Proc SPIE* **4253**, 176–188 (2001).
13. Liu XM, Cobb MJ, Chen YC et al. Rapid-scanning forward-imaging miniature endoscope for real-time optical coherence tomography. *Opt Lett* **29**, 1763–1765 (2004).
14. Kaur M, Lane PM, Menon C. Scanning and actuation techniques for cantilever-based fiber optic endoscopic scanners—a review. *Sensors* **21**, 251 (2021).
15. Kang JQ, Zhu R, Sun YX et al. Pencil-beam scanning catheter for intracoronary optical coherence tomography. *Opto-Electron Adv 5* **5**, 200050 (2022).
16. Hirschowitz BI, Curtiss LE, Peters CW et al. Demonstration of a new gastroscope, the "fiberscope". *Gastroenterology* **35**, 50–53 (1958).
17. Yan XQ, Li M, Chen ZQ et al. Schlemm's canal and trabecular meshwork in eyes with primary open angle glaucoma: a comparative study using high-frequency ultrasound biomicroscopy. *PLoS One* **11**, e0145824 (2016).
18. Kaur M, Lane PM, Menon C. Design of scanning fiber microcantilever based catheter for ultra-small endoscopes. In *Proceedings of 2023 IEEE World AI IoT Congress* 717–723 (IEEE, 2023);http://doi.org/10.1109/AIIoT58121.2023.10174425.
19. Chen XP, Reichenbach KL, Xu C. Experimental and theoretical analysis of core-to-core coupling on fiber bundle imaging. *Opt Express* **16**, 21598–21607 (2008).
20. Parker HE, Perperidis A, Stone JM et al. Core crosstalk in ordered imaging fiber bundles. *Opt Lett* **45**, 6490–6493 (2020).
21. Kyrish M, Kester R, Richards-Kortum R et al. Improving spatial resolution of a fiber bundle optical biopsy system. *Proc SPIE* **7558**, 755807 (2010).
22. Papadopoulos IN, Farahi S, Moser C et al. Focusing and scanning light through a multimode optical fiber using digital phase conjugation. *Opt Express* **20**, 10583–10590 (2012).
23. Čižmár T, Dholakia K. Shaping the light transmission through a multimode optical fibre: complex transformation analysis and applications in biophotonics. *Opt Express* **19**, 18871–18884 (2011).
24. Caravaca-Aguirre AM, Niv E, Conkey DB et al. Real-time resilient focusing through a bending multimode fiber. *Opt Express* **21**, 12881–12887 (2013).
25. Čižmár T, Dholakia K. Exploiting multimode waveguides for pure fibre-based imaging. *Nat Commun* **3**, 1027 (2012).
26. Di Leonardo R, Bianchi S. Hologram transmission through multi-mode optical fibers. *Opt Express* **19**, 247–254 (2011).
27. Zhao TR, Ourselin S, Vercauteren T et al. Seeing through multimode fibers with real-valued intensity transmission matrices. *Opt Express* **28**, 20978–20991 (2020).
28. Abraham E, Zhou JX, Liu ZW. Speckle structured illumination endoscopy with enhanced resolution at wide field of view and depth of field. *Opto-Electron Adv* **6**, 220163 (2023).
29. Choi Y, Yoon C, Kim M et al. Scanner-free and wide-field endoscopic imaging by using a single multimode optical fiber. *Phys Rev Lett* **109**, 203901 (2012).
30. Liu YF, Yu PP, Wu YJ et al. Single-shot wide-field imaging in reflection by using a single multimode fiber. *Appl Phys Lett* **122**, 063701 (2023).
31. Popoff S, Lerosey G, Fink M et al. Image transmission through an opaque material. *Nat Commun* **1**, 81 (2010).
32. Abrashitova K, Amitonova LV. High-speed label-free multimode-fiber-based compressive imaging beyond the diffraction limit. *Opt Express* **30**, 10456–10469 (2022).
33. Li SH, Saunders C, Lum DJ et al. Compressively sampling the optical transmission matrix of a multimode fibre. *Light Sci Appl* **10**, 88 (2021).
34. Amitonova LV, de Boer JF. Compressive imaging through a multimode fiber. *Opt Lett* **43**, 5427–5430 (2018).
35. Zhu RZ, Feng HG, Xu F. Deep learning-based multimode fiber imaging in multispectral and multipolarimetric channels. *Opt Lasers Eng* **161**, 107386 (2023).
36. Zhu RZ, Luo JX, Zhou XX et al. Anti-perturbation multimode fiber imaging based on the active measurement of the fiber configuration. *ACS Photonics* **10**, 3476–3483 (2023).
37. Xu RC, Zhang LH, Chen ZY et al. High accuracy transmission and recognition of complex images through multimode fibers using deep learning. *Laser Photonics Rev* **17**, 2200339 (2023).
38. Wang LL, Yang YS, Liu ZT et al. High‐speed all‐fiber micro‐imaging with large depth of field. *Laser Photonics Rev* **16**, 2100724 (2022).
39. Saleh BEA, Teich MC. *Fundamentals of Photonics* (Wiley, New York, 1991).
40. Xiong W, Hsu CW, Bromberg Y et al. Complete polarization control in multimode fibers with polarization and mode coupling. *Light Sci Appl* **7**, 54 (2018).
41. Popoff SM, Lerosey G, Carminati R et al. Measuring the transmission matrix in optics: an approach to the study and control of light propagation in disordered media. *Phys Rev Lett* **104**, 100601 (2010).
42. Turtaev S, Leite IT, Altwegg-Boussac T et al. High-fidelity multimode fibre-based endoscopy for deep brain in vivo imaging. *Light Sci Appl* **7**, 92 (2018).
43. Goorden SA, Bertolotti J, Mosk AP. Superpixel-based spatial amplitude and phase modulation using a digital micromirror device. *Opt Express* **22**, 17999–18009 (2014).
44. Dubois A, Vabre L, Boccara AC et al. High-resolution full-field optical coherence tomography with a Linnik microscope. *Appl Opt* **41**, 805–812 (2002).
45. Bianchi S, Di Leonardo R. A multi-mode fiber probe for holographic micromanipulation and microscopy. *Lab Chip* **12**, 635–639 (2012).
46. Conkey DB, Caravaca-Aguirre AM, Piestun R. High-speed scattering medium characterization with application to focusing light through turbid media. *Opt Express* **20**, 1733–1740 (2012).
47. Ivanina A, Lochocki B, Amitonova LV. Measuring the transmission matrix of a multimode fiber: on-axis vs off-axis holography. *Proc SPIE* **12574**, 125740T (2023).
48. Jákl P, Šiler M, Ježek J et al. Endoscopic imaging using a multimode optical fibre calibrated with multiple internal references. *Photonics* **9**, 37 (2022).
49. Jákl P, Šiler M, Ježek J et al. Multimode fiber transmission matrix obtained with internal references. *Proc SPIE* **10886**, 1088610 (2019).
50. Collard L, Piscopo L, Pisano F et al. Optimizing the internal phase reference to shape the output of a multimode optical fiber. *PLoS One* **18**, e0290300 (2023).
51. Amitonova LV, Mosk AP, Pinkse PWH. Rotational memory effect of a multimode fiber. *Opt Express* **23**, 20569–20575 (2015).
52. Li SH, Horsley SAR, Tyc T et al. Memory effect assisted imaging through multimode optical fibres. *Nat Commun* **12**, 3751 (2021).
53. Drémeau A, Liutkus A, Martina D et al. Reference-less measurement of the transmission matrix of a highly scattering material using a DMD and phase retrieval techniques. *Opt Ex-*

press **23**, 11898–11911 (2015).
54. N'Gom M, Norris TB, Michielssen E et al. Mode control in a multimode fiber through acquiring its transmission matrix from a reference-less optical system. *Opt Lett* **43**, 419–422 (2018).
55. Deng L, Yan JD, Elson DS et al. Characterization of an imaging multimode optical fiber using a digital micro-mirror device based single-beam system. *Opt Express* **26**, 18436–18447 (2018).
56. Caramazza P, Moran O, Murray-Smith R et al. Transmission of natural scene images through a multimode fibre. *Nat Commun* **10**, 2029 (2019).
57. Huang GQ, Wu DX, Luo JW et al. Retrieving the optical transmission matrix of a multimode fiber using the extended Kalman filter. *Opt Express* **28**, 9487–9500 (2020).
58. Tao XD, Bodington D, Reinig M et al. High-speed scanning interferometric focusing by fast measurement of binary transmission matrix for channel demixing. *Opt Express* **23**, 14168–14187 (2015).
59. Zhao TR, Deng L, Wang W et al. Bayes' theorem-based binary algorithm for fast reference-less calibration of a multimode fiber. *Opt Express* **26**, 20368–20378 (2018).
60. Zhao TR, Ourselin S, Vercauteren T et al. Focusing light through multimode fibres using a digital micromirror device: a comparison study of non-holographic approaches. *Opt Express* **29**, 14269–14281 (2021).
61. Plöschner M, Tyc T, Čižmár T. Seeing through chaos in multimode fibres. *Nat Photonics* **9**, 529–535 (2015).
62. Fischer B, Sternklar S. Image transmission and interferometry with multimode fibers using self‐pumped phase conjugation. *Appl Phys Lett* **46**, 113–114 (1985).
63. McMichael I, Yeh P, Beckwith P. Correction of polarization and modal scrambling in multimode fibers by phase conjugation. *Opt Lett* **12**, 507–509 (1987).
64. Son JY, Bobrinev VI, Jeon HW et al. Direct image transmission through a multimode optical fiber. *Appl Opt* **35**, 273–277 (1996).
65. Dunning GJ, Lind RC. Demonstration of image transmission through fibers by optical phase conjugation. *Opt Lett* **7**, 558–560 (1982).
66. Ogasawara T, Ohno M, Karaki K et al. Image transmission with a pair of graded-index optical fibers and a $BaTiO_3$ phase-conjugate mirror. *J Opt Soc Am B* **13**, 2193–2197 (1996).
67. Papadopoulos IN, Farahi S, Moser C et al. Focused light delivery and all optical scanning from a multimode optical fiber using digital phase conjugation. *Proc SPIE* **8576**, 857603 (2013).
68. Zhang JW, Ma CJ, Dai SQ et al. Transmission and total internal reflection integrated digital holographic microscopy. *Opt Lett* **41**, 3844–3847 (2016).
69. Ma CJ, Di JL, Li Y et al. Rotational scanning and multiple-spot focusing through a multimode fiber based on digital optical phase conjugation. *Appl Phys Express* **11**, 062501 (2018).
70. Papadopoulos IN, Farahi S, Moser C et al. High-resolution, lensless endoscope based on digital scanning through a multimode optical fiber. *Biomed Opt Express* **4**, 260–270 (2013).
71. Mididoddi CK, Lennon RA, Li SH et al. High-fidelity off-axis digital optical phase conjugation with transmission matrix assisted calibration. *Opt Express* **28**, 34692–34705 (2020).
72. Jang M, Ruan HW, Zhou HJ et al. Method for auto-alignment of digital optical phase conjugation systems based on digital propagation. *Opt Express* **22**, 14054–14071 (2014).
73. Mahalati RN, Askarov D, Wilde JP et al. Adaptive control of input field to achieve desired output intensity profile in multimode fiber with random mode coupling. *Opt Express* **20**, 14321–14337 (2012).
74. Zhao HC, Ma HT, Zhou P et al. Multimode fiber laser beam cleanup based on stochastic parallel gradient descent algorithm. *Opt Commun* **284**, 613–615 (2011).
75. Yu H, Yao ZY, Sui XB et al. Focusing through disturbed multimode optical fiber based on self-adaptive genetic algorithm. *Optik* **261**, 169129 (2022).
76. Cheng SF, Zhong TT, Woo CM et al. Long-distance pattern projection through an unfixed multimode fiber with natural evolution strategy-based wavefront shaping. *Opt Express* **30**, 32565–32576 (2022).
77. Li BQ, Zhang B, Feng Q et al. Shaping the wavefront of incident light with a strong robustness particle swarm optimization algorithm. *Chin Phys Lett* **35**, 124201 (2018).
78. Conkey DB, Brown AN, Caravaca-Aguirre AM et al. Genetic algorithm optimization for focusing through turbid media in noisy environments. *Opt Express* **20**, 4840–4849 (2012).
79. Yang ZG, Fang LJ, Zhang XC et al. Controlling a scattered field output of light passing through turbid medium using an improved ant colony optimization algorithm. *Opt Lasers Eng* **144**, 106646 (2021).
80. Fayyaz Z, Mohammadian N, Reza Rahimi Tabar M et al. A comparative study of optimization algorithms for wavefront shaping. *J Innov Opt Health Sci* **12**, 1942002 (2019).
81. Yin Z, Liu GD, Chen FD et al. Fast-forming focused spots through a multimode fiber based on an adaptive parallel coordinate algorithm. *Chin Opt Lett* **13**, 071404 (2015).
82. Chen H, Geng Y, Xu CF et al. Efficient light focusing through an MMF based on two-step phase shifting and parallel phase compensating. *Appl Opt* **58**, 7552–7557 (2019).
83. Zhang ZK, Kong DP, Geng Y et al. Lensless multimode fiber imaging based on wavefront shaping. *Appl Phys Express* **14**, 092002 (2021).
84. Gomes AD, Turtaev S, Du Y et al. Near perfect focusing through multimode fibres. *Opt Express* **30**, 10645–10663 (2022).
85. Choi Y, Yoon C, Kim M et al. Disorder-mediated enhancement of fiber numerical aperture. *Opt Lett* **38**, 2253–2255 (2013).
86. Papadopoulos IN, Farahi S, Moser C et al. Increasing the imaging capabilities of multimode fibers by exploiting the properties of highly scattering media. *Opt Lett* **38**, 2776–2778 (2013).
87. Jang H, Yoon C, Chung E et al. Holistic random encoding for imaging through multimode fibers. *Opt Express* **23**, 6705–6721 (2015).
88. Bianchi S, Rajamanickam VP, Ferrara L et al. Focusing and imaging with increased numerical apertures through multimode fibers with micro-fabricated optics. *Opt Lett* **38**, 4935–4938 (2013).
89. Amitonova LV, Descloux A, Petschulat J et al. High-resolution wavefront shaping with a photonic crystal fiber for multimode fiber imaging. *Opt Lett* **41**, 497–500 (2016).
90. Leite IT, Turtaev S, Jiang X et al. Three-dimensional holographic optical manipulation through a high-numerical-aperture soft-glass multimode fibre. *Nat Photonics* **12**, 33–39 (2018).
91. Stellinga D, Phillips DB, Mekhail SP et al. Time-of-flight 3D imaging through multimode optical fibers. *Science* **374**, 1395–1399 (2021).
92. Leite IT, Turtaev S, Boonzajer Flaes DE et al. Observing distant objects with a multimode fiber-based holographic endoscope. *APL Photonics* **6**, 036112 (2021).

93. Lyu ZP, Osnabrugge G, Pinkse PWH et al. Focus quality in raster-scan imaging via a multimode fiber. *Appl Opt* **61**, 4363–4369 (2022).
94. Descloux A, Amitonova LV, Pinkse PWH. Aberrations of the point spread function of a multimode fiber due to partial mode excitation. *Opt Express* **24**, 18501–18512 (2016).
95. Velsink MC, Lyu ZY, Pinkse PWH et al. Comparison of round- and square-core fibers for sensing, imaging, and spectroscopy. *Opt Express* **29**, 6523–6531 (2021).
96. Turcotte R, Sutu E, Schmidt CC et al. Deconvolution for multimode fiber imaging: modeling of spatially variant PSF. *Biomed Opt Express* **11**, 4759–4771 (2020).
97. Turcotte R, Schmidt CC, Emptage NJ et al. Focusing light in biological tissue through a multimode optical fiber: refractive index matching. *Opt Lett* **44**, 2386–2389 (2019).
98. Laporte GPJ, Stasio N, Moser C et al. Enhanced resolution in a multimode fiber imaging system. *Opt Express* **23**, 27484–27493 (2015).
99. Loterie D, Farahi S, Papadopoulos I et al. Digital confocal microscopy through a multimode fiber. *Opt Express* **23**, 23845–23858 (2015).
100. Webb RH. Confocal optical microscopy. *Rep Prog Phys* **59**, 427–471 (1996).
101. Tučková T, Šiler M, Flaes DEB et al. Computational image enhancement of multimode fibre-based holographic endo-microscopy: harnessing the *muddy modes*. *Opt Express* **29**, 38206–38220 (2021).
102. Turtaev S, Leite IT, Mitchell KJ et al. Comparison of nematic liquid-crystal and DMD based spatial light modulation in complex photonics. *Opt Express* **25**, 29874–29884 (2017).
103. Zhang XH, Wen Z, Ma YG et al. High contrast multimode fiber imaging based on wavelength modulation. *Appl Opt* **59**, 6677–6681 (2020).
104. Plöschner M, Straka B, Dholakia K et al. GPU accelerated toolbox for real-time beam-shaping in multimode fibres. *Opt Express* **22**, 2933–2947 (2014).
105. Plöschner M, Čižmár T. Compact multimode fiber beam-shaping system based on GPU accelerated digital holography. *Opt Lett* **40**, 197–200 (2015).
106. Lee WH. Binary computer-generated holograms. *Appl Opt* **18**, 3661–3669 (1979).
107. Stellinga D, Phillip DB, Mekhail S et al. 3D imaging through a single optical fiber. *Proc SPIE* **12016**, 120160M (2022).
108. Turtaev S, Leite IT, Mitchell KJ et al. Exploiting digital micromirror device for holographic micro-endoscopy. *Proc SPIE* **10932**, 1093203 (2019).
109. Turtaev S, Leite IT, Cizmar T. Liquid-crystal and MEMS modulators for beam-shaping through multimode fibre. In *Proceedings of 2018 IEEE Photonics Society Summer Topical Meeting Series* 207–208 (IEEE, 2018); http://doi.org/10.1109/PHOSST.2018.8456776.
110. Caravaca-Aguirre AM, Piestun R. Single multimode fiber endoscope. *Opt Express* **25**, 1656–1665 (2017).
111. Amitonova LV, de Boer JF. Endo-microscopy beyond the Abbe and Nyquist limits. *Light Sci Appl* **9**, 81 (2020).
112. Zhu RZ, Feng HG, Xiong YF et al. All-fiber reflective single-pixel imaging with long working distance. *Opt Laser Technol* **158**, 108909 (2023).
113. Wu YC, Rivenson Y, Wang HD et al. Three-dimensional virtual refocusing of fluorescence microscopy images using deep learning. *Nat Methods* **16**, 1323–1331 (2019).
114. Wen Z, Dong ZY, Deng QL et al. Single multimode fibre for in vivo light-field-encoded endoscopic imaging. *Nat Photonics* **17**, 679–687 (2023).
115. Olshansky R. Mode coupling effects in graded-index optical fibers. *Appl Opt* **14**, 935–945 (1975).
116. Flaes DEB, Stopka J, Turtaev S et al. Robustness of light-transport processes to bending deformations in graded-index multimode waveguides. *Phys Rev Lett* **120**, 233901 (2018).
117. Loterie D, Psaltis D, Moser C. Bend translation in multimode fiber imaging. *Opt Express* **25**, 6263–6273 (2017).
118. Farahi S, Ziegler D, Papadopoulos IN et al. Dynamic bending compensation while focusing through a multimode fiber. *Opt Express* **21**, 22504–22514 (2013).
119. Gu RY, Mahalati RN, Kahn JM. Design of flexible multi-mode fiber endoscope. *Opt Express* **23**, 26905–26918 (2015).
120. Gordon GSD, Gataric M, Ramos AGCP et al. Characterizing optical fiber transmission matrices using metasurface reflector stacks for lensless imaging without distal access. *Phys Rev X* **9**, 041050 (2019).
121. Chen HS, Fontaine NK, Ryf R et al. Remote spatio-temporal focusing over multimode fiber enabled by single-ended channel estimation. *IEEE J Sel Top Quantum Electron* **26**, 7701809 (2020).
122. Wen Z, Wang LQ, Zhang XH et al. Fast volumetric fluorescence imaging with multimode fibers. *Opt Lett* **45**, 4931–4934 (2020).
123. Schmidt CC, Turcotte R, Booth MJ et al. Repeated imaging through a multimode optical fiber using adaptive optics. *Biomed Opt Express* **13**, 662–675 (2022).
124. Rudolf B, Du Y, Turtaev S et al. Thermal stability of wavefront shaping using a DMD as a spatial light modulator. *Opt Express* **29**, 41808–41818 (2021).
125. Zhou Y, Hong MH. Realization of noncontact confocal optical microsphere imaging microscope. *Microsc Res Tech* **84**, 2381–2387 (2021).
126. Yang XL, Hong MH. Enhancement of axial resolution and image contrast of a confocal microscope by a microsphere working in noncontact mode. *Appl Opt* **60**, 5271–5277 (2021).
127. Loterie D, Goorden SA, Psaltis D et al. Confocal microscopy through a multimode fiber using optical correlation. *Opt Lett* **40**, 5754–5757 (2015).
128. Singh S, Labouesse S, Piestun R. Multiview virtual confocal microscopy through a multimode fiber. In *Proceedings of 2021 IEEE 18th International Symposium on Biomedical Imaging* 584–587 (IEEE, 2021); http://doi.org/10.1109/ISBI48211.2021.9433950.
129. Singh S, Labouesse S, Piestun R. Multiview scattering scanning imaging confocal microscopy through a multimode fiber. *IEEE Trans Comput Imaging* **9**, 159–171 (2023).
130. Loterie D, Psaltis D, Moser C. Confocal microscopy via multimode fibers: fluorescence bandwidth. *Proc SPIE* **9717**, 97171C (2016).
131. So PTC, Dong CY, Masters BR et al. Two-photon excitation fluorescence microscopy. *Annu Rev Biomed Eng* **2**, 399–429 (2000).
132. Cao H, Čižmár T, Turtaev S et al. Controlling light propagation in multimode fibers for imaging, spectroscopy, and beyond. *Adv Opt Photonics* **15**, 524–612 (2023).
133. Xiong W, Ambichl P, Bromberg Y et al. Spatiotemporal control of light transmission through a multimode fiber with strong mode coupling. *Phys Rev Lett* **117**, 053901 (2016).
134. Xiong W, Hsu CW, Cao H. Long-range spatio-temporal correlations in multimode fibers for pulse delivery. *Nat Commun* **10**,

2973 (2019).
135. Morales-Delgado EE, Farahi S, Papadopoulos IN et al. Delivery of focused short pulses through a multimode fiber. *Opt Express* **23**, 9109–9120 (2015).
136. Morales-Delgado EE, Psaltis D, Moser C. Two-photon imaging through a multimode fiber. *Opt Express* **23**, 32158–32170 (2015).
137. Pikálek T, Trägårdh J, Simpson S et al. Wavelength dependent characterization of a multimode fibre endoscope. *Opt Express* **27**, 28239–28253 (2019).
138. Trägårdh J, Pikálek T, Simpson S et al. Towards focusing broad band light through a multimode fiber endoscope. *Proc SPIE* **10886**, 108860J (2019).
139. Turcotte R, Schmidt CC, Booth MJ et al. Volumetric two-photon fluorescence imaging of live neurons using a multimode optical fiber. *Opt Lett* **45**, 6599–6602 (2020).
140. Sivankutty S, Andresen ER, Cossart R et al. Ultra-thin rigid endoscope: two-photon imaging through a graded-index multimode fiber. *Opt Express* **24**, 825–841 (2016).
141. Velsink MC, Amitonova LV, Pinkse PWH. Spatiotemporal focusing through a multimode fiber via time-domain wavefront shaping. *Opt Express* **29**, 272–290 (2021).
142. Gusachenko I, Chen MZ, Dholakia K. Raman imaging through a single multimode fibre. *Opt Express* **25**, 13782–13798 (2017).
143. Gusachenko I, Nylk J, Tello JA et al. Multimode fibre based imaging for optically cleared samples. *Biomed Opt Express* **8**, 5179–5190 (2017).
144. Deng SN, Loterie D, Konstantinou G et al. Raman imaging through multimode sapphire fiber. *Opt Express* **27**, 1090–1098 (2019).
145. Zhang C, Aldana-Mendoza JA. Coherent Raman scattering microscopy for chemical imaging of biological systems. *J Phys Photonics* **3**, 032002 (2021).
146. Trägårdh J, Pikálek T, Šerý M et al. Label-free CARS microscopy through a multimode fiber endoscope. *Opt Express* **27**, 30055–30066 (2019).
147. Pikálek T, Stibůrek M, Simpson S et al. Suppression of the non-linear background in a multimode fibre CARS endoscope. *Biomed Opt Express* **13**, 862–874 (2022).
148. Cifuentes A, Pikálek T, Ondráčková P et al. Polarization-resolved second-harmonic generation imaging through a multimode fiber. *Optica* **8**, 1065–1074 (2021).
149. Yang LY, Li YP, Fang F et al. Highly sensitive and miniature microfiber-based ultrasound sensor for photoacoustic tomography. *Opto-Electron Adv* **5**, 200076 (2022).
150. Mezil S, Caravaca-Aguirre AM, Zhang EZ et al. Single-shot hybrid photoacoustic-fluorescent microendoscopy through a multimode fiber with wavefront shaping. *Biomed Opt Express* **11**, 5717–5727 (2020).
151. Zhao TR, Ma MT, Ourselin S et al. Video-rate dual-modal photoacoustic and fluorescence imaging through a multimode fibre towards forward-viewing endomicroscopy. *Photoacoustics* **25**, 100323 (2022).
152. Zhao TR, Pham TT, Baker C et al. Ultrathin, high-speed, all-optical photoacoustic endomicroscopy probe for guiding minimally invasive surgery. *Biomed Opt Express* **13**, 4414–4428 (2022).
153. Zhao TR, Zhang MJ, Ourselin S et al. Wavefront shaping-assisted forward-viewing photoacoustic endomicroscopy based on a transparent ultrasound sensor. *Appl Sci* **12**, 12619 (2022).
154. Zhao TR, Shi MJ, Ourselin S et al. Deep learning boosts the imaging speed of photoacoustic endomicroscopy. *Proc SPIE* **12379**, 123790J (2023).
155. Ohayon S, Caravaca-Aguirre A, Piestun R et al. Minimally invasive multimode optical fiber microendoscope for deep brain fluorescence imaging. *Biomed Opt Express* **9**, 1492–1509 (2018).
156. Kakkava E, Romito M, Conkey DB et al. Selective femtosecond laser ablation via two-photon fluorescence imaging through a multimode fiber. *Biomed Opt Express* **10**, 423–433 (2019).
157. Stibůrek M, Ondráčková P, Tučková T et al. 110 μm thin endomicroscope for deep-brain in vivo observations of neuronal connectivity, activity and blood flow dynamics. *Nat Commun* **14**, 1897 (2023).
158. Karbasi S, Frazier RJ, Koch KW et al. Image transport through a disordered optical fibre mediated by transverse Anderson localization. *Nat Commun* **5**, 3362 (2014).
159. Rivenson Y, Göröcs Z, Günaydin H et al. Deep learning microscopy. *Optica* **4**, 1437–1443 (2017).
160. Qiao C, Li D, Liu Y et al. Rationalized deep learning super-resolution microscopy for sustained live imaging of rapid subcellular processes. *Nat Biotechnol* **41**, 367–377 (2023).

Acknowledgements

This work was supported by National Natural Science Foundation of China (62135007 and 61925502).

Competing interests

Minghui Hong serves as an Editor for the Journal, no other author has reported any competing interests.

Scan for Article PDF